IMA Journal of Numerical Analysis (2021) **00**, 1–34
doi:10.1093/imanum/drab007

The numerical unified transform method for initial-boundary value problems on the half-line

BERNARD DECONINCK, THOMAS TROGDON AND XIN YANG*
Department of Applied Mathematics, University of Washington, Seattle, WA 98195, USA
*Corresponding author: yangxin@uw.edu

[Received on 10 June 2020; revised on 10 December 2020]

We implement the unified transform method of Fokas as a numerical method to solve linear evolution partial differential equations on the half-line. The method computes the solution at any x and t without spatial discretization or time stepping. With the help of contour deformations and oscillatory integration techniques, the method's complexity does not increase for large x, t and the method is more accurate as x, t increase (absolute errors are smaller, relative errors are bounded). Our goal is to make no assumptions on the functional form of the initial or boundary functions beyond some decay and smoothness, while maintaining high accuracy in a large region of the (x, t) plane.

Keywords: linear evolution partial differential equations; numerical unified transform method; method of steepest descent; numerical oscillatory integrals.

1. Introduction

Standard methods for solving linear evolution partial differential equations (PDEs), including separation of variables and classical integral transforms, are often limited by the order of the PDE and the type of boundary conditions. The unified transform method (UTM), also known as the method of Fokas (Fokas, 1997), is a relatively new method for analysing a large family of PDEs with general initial and boundary conditions (Fokas, 2002a). When applied to initial boundary value problems (IBVPs) for linear, constant coefficient PDEs, the UTM provides the solutions in terms of contour integrals involving the given initial and boundary conditions (Deconinck *et al.*, 2014). This does not only give rise to new analysis, but it also provides a new direction for numerical methods. With this integral representation of the solution it is possible to compute the solution at any x, t directly. The numerical UTM (NUTM) is a numerical method built upon the solution formula from the UTM with the addition of systematic contour deformations. In stark contrast to classical numerical PDE methods such as finite-difference methods, most spectral methods and finite-element methods the NUTM can solve equations in unbounded domains, and it does not experience accumulation of errors or stability issues. These issues that appear in standard numerical methods for evolution PDEs do not appear in the NUTM because spatial discretization and time stepping are not required. As a hybrid analytical-numerical method the NUTM operates in a complementary direction to the traditional numerical methods. In practice, if one is interested in the solution on a dense spacial and temporal grid and is satisfied with lower accuracy, traditional methods are better choices, whereas if one is interested in the solution along some curve with high accuracy for a long time, the NUTM is likely better. On the other hand, the NUTM can act as a benchmark tool for other numerical methods.

Since the first paper on the NUTM in 2008 (Flyer & Fokas, 2008) the method has been applied to the heat equation $q_t = q_{xx}$ on the half-line (Flyer & Fokas, 2008; Fokas *et al.*, 2009) and on finite intervals

(Papatheodorou & Kandili, 2009), to the Stokes equations $q_t \pm q_{xxx} = 0$ on the half-line (Flyer & Fokas, 2008) and on finite intervals (Kesici *et al.*, 2018) and the advection-diffusion equation $q_t + q_x = q_{xx}$ on the half-line (de Barros *et al.*, 2019). These applications of the NUTM use fixed contours that do not depend on (x, t), and most of them[1] rely on knowing closed-form expressions for the transforms of initial and boundary data. We refer to such implementations of the NUTM as fixed contour methods (FCMs). As we will see in Section 3.3 FCMs become less accurate for large x, t.

In contrast to those FCMs we propose a new implementation of the NUTM that uses contours depending dynamically on x, t, and that does not severely restrict the initial or boundary conditions. Our goal is to make no assumptions on the functional form of the initial or boundary functions, other than to restrict them to be in certain function spaces (i.e., impose specific decay). We maintain high accuracy in a large region of the (x, t) plane. To summarize, we build up the NUTM to include the following features:

1. The assumptions on the initial and boundary conditions are significantly weakened compared to the FCM. Decay and regularity conditions are necessary for the purpose of achieving high accuracy. We emphasize that closed-form expressions for the transforms of initial or boundary conditions are not required.

2. The method is uniformly accurate in that the computational cost to compute the solution at a point (x, t) with given accuracy remains bounded for large x, t. In addition, we observe bounded relative errors in our numerical experiments.

3. The method is spectrally accurate in that the error at fixed (x, t), $E_{\mathrm{NUTM}}(N, x, t) = \mathcal{O}(1/N^l)$ for any integer l, where N is the number of function evaluations. For certain equations such as the heat equation, it is possible to achieve spectral accuracy uniformly as long as (x, t) are bounded away from $x = 0$ and $t = 0$.

These features exist in the numerical inverse scattering transform we have implemented for nonlinear integrable PDEs on the whole line (Trogdon *et al.*, 2012; Trogdon & Olver, 2013; Deconinck *et al.*, 2019). Having studied the solution of the IVP of nonlinear integrable equations and the solution of the IBVP of linear constant coefficient equations, we are set up to understand the numerical issues associated with IBVPs for nonlinear integrable PDEs Fokas (2002b, 2005). Ultimately, we wish to compute the solution of the IBVP of nonlinear integrable equations using the NUTM in a similar fashion.

In this paper we consider linear, constant coefficient, one-dimensional scalar evolution equations with $x > 0$. Further generalizations are left for future projects. The paper is organized as follows: Section 2 gives a brief overview of the UTM and the methods for oscillatory integrals that are required in what follows. In Section 3, we discuss the NUTM for the heat equation where the deformation is based on the method of steepest descent. In Section 4, we discuss the NUTM applied to the linear Schrödinger (LS) equation, where methods other than the method of steepest descent are needed. In Section 5, we show how to apply the NUTM to a third-order PDE with an advection term giving rise to integrands with branch points. We believe that the best way to explain the NUTM, similar to introducing the UTM, is to use a case-by-case study. In Section 6, we summarize the steps of the NUTM.

Numerical examples are provided throughout. In many examples, the initial and boundary conditions are chosen to have closed-form transforms for the purpose of computing the true solution for

---

[1] In de Barros *et al.* (2019), one numerical example without closed-form expressions for the transforms is considered, but the idea is not applied to nondissipative problems.

comparison. An example with the boundary condition that does not have a known expression for the transform is shown at the end of Section 5.2. The proof of the uniform convergence of the NUTM applied to the heat equation is given in the appendix.

2. Preliminaries

2.1 *The UTM on the half-line*

Consider a linear PDE written as

$$q_t + \omega(-i\partial_x)q = 0, \tag{1}$$

for $x, t > 0$. We assume $\omega(k)$ to be a polynomial of degree p. Note that $q(x,t) = e^{ikx-\omega(k)t}$ satisfies (1). This definition of the dispersion relation ω typically used in the UTM differs from the common convention by a factor of i. The UTM solves IBVPs for (1) using transforms of the initial and boundary values:

$$\hat{q}_0(k) = \int_0^\infty e^{-ikx} q_0(x,0)\,\mathrm{d}x, \tag{2}$$

$$\tilde{g}_0(\omega(k),t) = \int_0^t e^{\omega(k)s} q(0,s)\,\mathrm{d}s, \tag{3}$$

$$\vdots$$

$$\tilde{g}_{p-1}(\omega(k),t) = \int_0^t e^{\omega(k)s} \frac{\partial^{p-1}q}{\partial x^{p-1}}(0,s)\,\mathrm{d}s. \tag{4}$$

The number of boundary conditions required for a well-posed problem is determined by the UTM. It is based on the order of the highest spatial derivative as well as the leading coefficient of ω (Flyer & Fokas, 2008). The solution formula from the UTM depends on contour integrals of the type

$$I_m = \int_{\mathcal{C}_m^I} e^{ikx-w(k)t}\hat{q}_0(\nu_m(k))\,\mathrm{d}k, \quad m = 1,2,\ldots,p,$$

$$B_m = \int_{\mathcal{C}_m^B} e^{ikx-w(k)t} f_m(k)\hat{g}_m(\omega(k),t)\,\mathrm{d}k, \quad m = 0,1,\ldots,n,$$

where p is the degree of $\omega(k)$ and $\nu_m(k)$ is its mth symmetry[2], and $f_m(k)$ is a function explicitly determined by $\omega(k)$, independent of the initial and boundary data. Thus, the solution to (1) can be computed by quadrature. However, the integrands on the contours $\mathcal{C}_m^I$ and $\mathcal{C}_m^B$ obtained by the UTM are often highly oscillatory, and suitable methods must be applied for an accurate solution.

---

[2] A symmetry $\nu(k)$ of $\omega(k)$ satisfies $\omega(\nu(k)) = \omega(k)$. The symmetries play an important role in the UTM. The n symmetries $\{\nu_m(k) : m = 1,2,\ldots,n\}$ exist by the fundamental theorem of algebra and can be chosen to be analytic outside a compact set (Fokas, 2008).

2.2 *Methods for oscillatory integrals*

The exponential factor $e^{ikx-w(k)t}$ in the integrand is the main cause of oscillations. Deformations based on the method of steepest descent (Miller, 2006) change the oscillations into exponential decay. Define the phase function $\theta(k;x,t) = ikx - w(k)t$. Saddle points k_0 satisfy

$$\frac{d\theta(k;x,t)}{\mathrm{d}k}\bigg|_{k=k_0} = 0.$$

Near $k = k_0$,

$$\theta(k;x,t) = ik_0x - w(k_0)t - \frac{w''(k_0)t}{2}(k-k_0)^2 + \mathcal{O}(k-k_0)^3.$$

The integrand is (locally) exponentially decaying if k follows a path such that $-w''(k_0)(k-k_0)^2$ is negative and decreasing. Since the integrals along the deformed paths are exponentially localized near the saddle point, they can be computed with high accuracy with standard quadrature methods after appropriate truncation.

For improved accuracy, Gauss–Hermite or Gauss–Laguerre quadratures are suitable, depending on the form of the exponentials and the paths (Huybrechs & Gibbs; Uspensky, 1928; Gibbs *et al.*, 2020). We choose Clenshaw–Curtis quadrature for the deformed contour integrals for convenience, as it is spectrally accurate and efficient in most cases (Trefethen, 2008). We note that there are situations where the deformations are restricted and the method of steepest descent is not applicable, see Sections 4 and 5.

The region in the complex k-plane where the contour can be deformed depends on the analyticity of the transform data $\hat{q}_0(k)$ and $\hat{g}_m(\omega(k),t)$, which is related to the decay rate of the initial and boundary data. For instance, when $q(x,0)$ and $q(0,t)$ are integrable, $\hat{q}_0$ is analytic and bounded in the lower-half plane $\{k \in \mathbb{C} : \mathrm{Im}\,(k) < 0\}$ and $\hat{g}_0(\omega(k),t)$ is analytic and bounded in $\{k \in \mathbb{C} : \mathrm{Re}\,(\omega(k)) < 0\}$. Data with faster decay give more freedom to deform the contour. We consider data with exponential decay rate $\delta > 0$, defined by

$$C^m_\delta = \left\{ f \in C^m([0,\infty)),\ \exists \delta' > \delta,\ \text{such that} \sup_{x\in[0,\infty)} e^{\delta' x}|f(x)| < \infty \right\}.$$

Remark. For $f \in C^m_\delta$ we have $\int_0^\infty e^{\delta'' x}|f(x)|\,\mathrm{d}x < \infty$ with $\delta'' = \frac{\delta'+\delta}{2} > \delta$. The boundedness is introduced for convenience in the proofs in the appendix, and the implied integrability is used to allow deformation of contours, not just in the interior of regions, but also to their boundaries.

If the initial condition $q_0 \in C^m_\delta$ then $\hat{q}_0$ is analytic and bounded in a open set containing $\{k \in \mathbb{C} : \mathrm{Im}\,(k) \le \delta\}$. Therefore, contour integrals of $\hat{q}_0(k)$ can be deformed inside a larger region. When the contours get close to the boundary of regions in which they can be deformed highly oscillatory integrals of the form

$$S(x,t) = \int_{k_0}^\infty f(k)\, e^{\theta(k;x,t)}\,\mathrm{d}k, \tag{5}$$

appear. Here $f(k)$ is, in general, not analytically extendable off the real axis, $k = k_0$ is the critical point of $\theta(k;x,t)$ and $\omega(k) \in i\mathbb{R}$. This integral is highly oscillatory when the parameters x, t are large, and therefore with traditional numerical quadrature methods the cost to achieve a desired accuracy increases as x, t increase. Fortunately, there are methods specific to highly oscillatory integrals, such as Filon-type and Levin-type methods, that are more accurate as oscillations increase, with a fixed number of evaluations of the integrand. Hence, it is still possible to attain uniform accuracy without increasing computational cost. Readers can check (Iserles *et al.*, 2006, Section 3.3) that has a nice and concise description of how Levin's method works. On the other hand, unlike in the method of steepest descent, the global error over all x, t does not, in general, decay spectrally. While we do compute solutions at arbitrarily large x, t with increasing accuracy, as x, t increase improvements over our methodology in the computation of integrals of the type given in (5) will improve the overall efficiency of our method. Some possible directions for the improved evaluation of (5) are as follows:

1. Better computational methods for oscillatory integrals that can achieve higher order of accuracy.
2. Faster solvers that can handle more nodes/modes in Levin-type methods like the ultraspherical polynomial spectral method (Olver & Townsend, 2012).

We emphasize that our work focuses on the integrals from the UTM, and therefore we focus on analyticity and decay of the integrands and possible contour deformations. A complete discussion of the treatment of (5) is beyond the scope of this paper, as any improvement is not only relevant to the NUTM, but is also worth studying for its own sake.

In order to make use of the path of steepest descent to obtain exponential localization, we avoid computing the solution with arbitrarily small x or t. Hence, in discussion about uniform accuracy, we assume $x, t \geq c$ for some constant $c > 0$. We choose $c = 0.1$ in most examples for convenience.

REMARK. The NUTM is less efficient for small x or t. We can use extrapolation and Taylor expansions to get $q(x, t)$ with small x or t (Trogdon & Biondini, 2019). Traditional time-stepping methods can be powerful and convenient if the number of time steps is small.

Methods for oscillatory integrals are also needed for computing the transforms $\hat{q}, \tilde{g}$. These transformed data are Fourier-type integrals that can be handled efficiently by Levin's method. In Fig. 1, the absolute errors for $\hat{q}_0(x + i)$ for $q_0(x) = e^{-2x}$ are plotted. The number of collocation points $N = 40$ is the same for Levin's method and for Clenshaw–Curtis quadrature. The values start to diverge for large x for Clenshaw–Curtis quadrature when the oscillations are under resolved, but Levin's method provides reliable approximations with decreasing errors.

3. The heat equation on the half-line

We consider the heat equation on the half-line,

$$q_t = q_{xx}, \quad t > 0, \quad x > 0, \tag{6}$$

with Dirichlet boundary data $q(0, t) = g_0(t)$ and initial data $q(x, 0) = q_0(x)$. The dispersion relation for the heat equation is $\omega(k) = k^2$. The initial data q_0 are assumed to be in C^∞_δ for some $\delta > 0$, and the boundary data g_0 are assumed to be in C^∞_γ for some $\gamma > 0$. The smoothness of q_0, g_0 allows us to compute the transformed data $\hat{q}$, $\tilde{g}$ accurately. The rate of decay affects the regions where the deformation of the integration path is allowed. The same methodology can still be applied, with less efficiency and accuracy, when weaker conditions are satisfied.

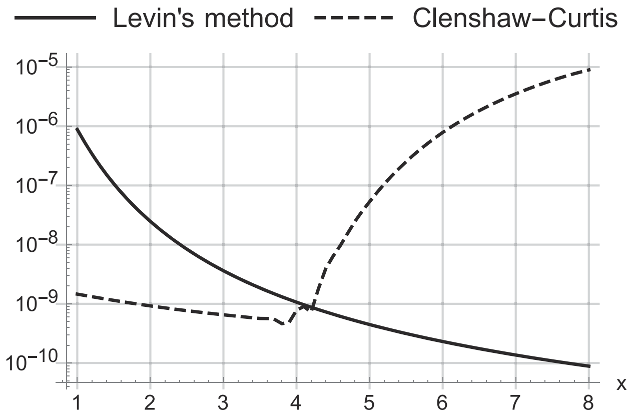

FIG. 1. The absolute errors for the computation of $\hat{q}_0(x+i)$ for $x \in [1,8]$. The curves are computed using Clenshaw–Curtis quadrature (dashed) and Levin's method (solid). Both methods use a fixed number of nodes $N = 40$. The initial data is $q_0(x) = e^{-2x}$.

REMARK. It is possible to deal with nondecaying boundary data when the asymptotics of the data is known and can be handled by some other method. The UTM for linear PDEs with piecewise-constant data is studied in Trogdon & Biondini (2019). Since the equation is linear, if the data is given as a superposition of data, it may then be beneficial to obtain the solution of the full problem as a superposition of solutions corresponding to individual pieces of data. For instance, suppose $g_0(t) = h_1 + h_2(t)$ where h_1 is a constant and $h_2 \in C_\delta^\infty$. The transform $\hat{h}_1(k,\infty) = -1/k^2$ is a meromorphic function in $\mathbb{C}$, and there is no restriction about where the integral contour for $\hat{h}_1(k,\infty)$ can be deformed if the residue is collected correctly. The full solution is easily obtained by superimposing the NUTM solutions for the problems corresponding to h_1 and h_2 separately.

3.1 *The solution formula from the UTM*

The solution to the heat equations on the half-line with Dirichlet boundary condition is given by Fokas (2008)

$$q(x,t) = \frac{1}{2\pi}\int_{-\infty}^{\infty} e^{ikx-\omega(k)t}\hat{q}_0(k)\,\mathrm{d}k - \frac{1}{2\pi}\int_{\partial D^+} e^{ikx-\omega(k)t}\left[\hat{q}_0(-k) + 2ik\tilde{g}_0(\omega(k),t)\right]\mathrm{d}k, \tag{7}$$

where the contour $\partial D^+ = \{re^{i\pi/4} : r \in [0,\infty)\} \cup \{re^{3i\pi/4} : r \in [0,\infty)\}$ is the boundary of the region $D^+ = \{(re^{iu}) : r \in (0,\infty), u \in (\pi/4, 3\pi/4)\}$, shown in Fig. 2a. The transformed data $\hat{q}_0(k)$ and $\tilde{g}_0(\omega(k),t)$ are defined by (2) and (4), respectively.

Using the classical sine transform Deconinck *et al.* (2014), a different representation of the solution is

$$q(x,t) = \frac{2}{\pi}\int_0^{\infty} e^{-\omega(k)t}\sin(kx)\left[\sin(ky)q(y,0)\,\mathrm{d}y - k\tilde{g}_0(\omega(k),t)\right]\mathrm{d}k. \tag{8}$$

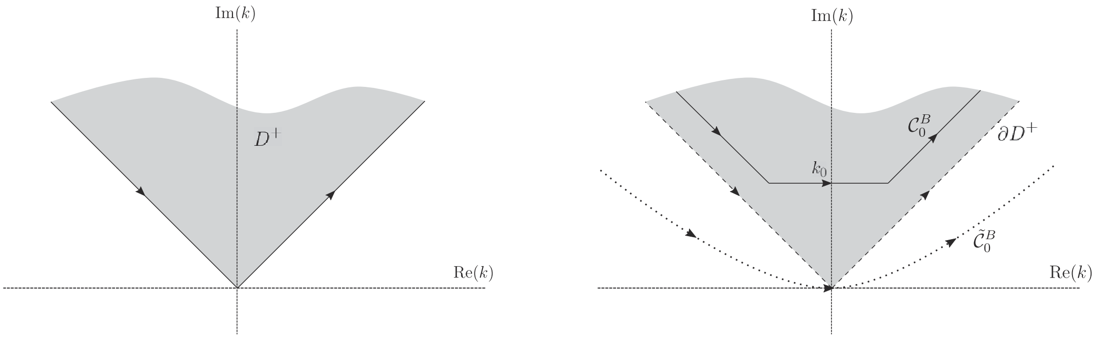

(a) (b)

FIG. 2. Regions for the heat equation. Panel (a) shows the region $D^+ = \{\mathrm{Re}(k^2) < 0\} \cap \mathbb{C}^+$. Panel (b) shows different integral paths for B_0: (i) ∂D^+: the undeformed contour (dashed), (ii) $\mathcal{C}_0^B$: the deformed contour across the saddle point k_0 (solid) and (iii) $\tilde{\mathcal{C}}_0^B$: the deformed contour used in Flyer & Fokas (2008) (dotted).

The equivalence of the expressions is shown by deforming the contour of (7) back to the real line. The reason we do not work with (8) is twofold:

1. Deforming the contour back to the real axis is possible only when classical transforms exist. Generally speaking, classical transforms do not exist for dispersive equations.
2. It is more straightforward to apply the method of steepest descent numerically to (7) than it is to (8).

3.2 *Deformations of contours based on the method of steepest descent*

We write the solution (7) as

$$q(x,t) = I_1 + I_2 + B_0, \tag{9}$$

where

$$\begin{aligned} I_1 &= \frac{1}{2\pi}\int_{-\infty}^{\infty} e^{ikx-\omega(k)t}\hat{q}_0(k)\,\mathrm{d}k, \\ I_2 &= -\frac{1}{2\pi}\int_{\partial D^+} e^{ikx-\omega(k)t}\hat{q}_0(-k)\,\mathrm{d}k, \\ B_0 &= -\frac{1}{2\pi}\int_{\partial D^+} e^{ikx-\omega(k)t}2ik\tilde{g}_0(\omega(k),t)\,\mathrm{d}k. \end{aligned}$$

The associated deformed contours for I_1, I_2 and B_0 will be defined by $\mathcal{C}_1^I, \mathcal{C}_2^I$ and $\mathcal{C}_0^B$, respectively, in the following sections. In Flyer & Fokas (2008), for the FCM, the deformed contour $\tilde{\mathcal{C}}_0^B$ is independent of (x,t), and is the same for all three integrals I_1, I_2 and B_0. The contour $\tilde{\mathcal{C}}_0^B$ is a hyperbola parameterized

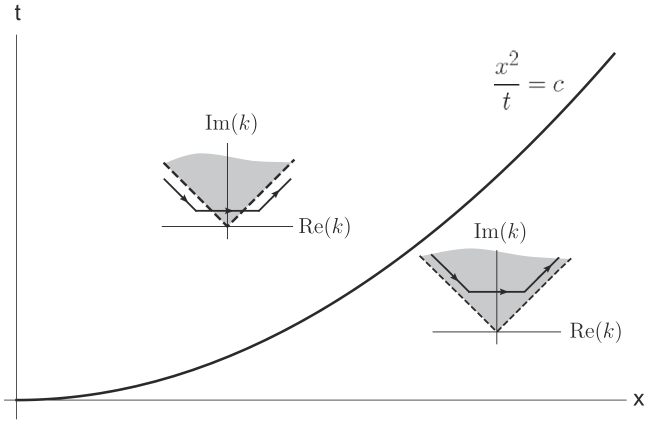

FIG. 3. Deformed contours for the heat equation. Depending on the values of (x, t), the deformed contour for B_0 can be inside or outside of ∂D^+. Solid lines represent the deformed contours. Dashed lines give ∂D^+, where D^+ is the shaded region. See Section 3.2.3 for a detailed description of these deformations.

by $s \in \mathbb{R}$, shown in Fig. 2,

$$k(s) = i \sin(\pi/8 - is). \tag{10}$$

This contour $\tilde{\mathcal{C}}_0^B$ is also used in Fokas *et al.* (2009), Papatheodorou & Kandili (2009) and de Barros *et al.* (2019) for different types of advection-diffusion equations. There are two major drawbacks of using $\tilde{\mathcal{C}}_0^B$: (i) the integrands of I_1, B_0 are not defined on all of $\tilde{\mathcal{C}}_0^B$, and (ii) the evaluation of the integral along $\tilde{\mathcal{C}}_0^B$ quickly loses accuracy when t increases, as it does not follow the direction of steepest descent, and large oscillations and potential growth destroy accuracy. To fix these issues with FCMs we use different deformations of the contours for I_0, I_1 and B_0 that depend on (x, t), and the contours are deformed to follow the direction of steepest descent as much as possible, see Fig. 3.

3.2.1 *I_1: the integral involving $\hat{q}_0(k)$.* The phase function in the integrand is

$$\theta(k; x, t) = ikx - \omega(k)t = ikx - k^2 t. \tag{11}$$

There is one saddle point $k_0 = ix/2t$ where $\theta'(k_0; x, t) = 0$ on the imaginary axis. The phase function $\theta(k; x, t)$ can be rewritten as

$$\theta(k; x, t) = ikx - k^2 t = -t(k - ix/2t)^2 - x^2/4t.$$

The direction of steepest descent, along which the magnitude of $e^{\theta(k;x,t)}$ decays exponentially, is horizontal. If $\mathrm{Im}(k_0) = x/2t > \delta$, the contour cannot be deformed to pass through the saddle point k_0 because the transform of the initial data $q \in C_\delta^\infty$ is only guaranteed to be defined for $\mathrm{Im}(k) \leq \delta$. However, there is exponential decay in the integrand when the path is along the horizontal

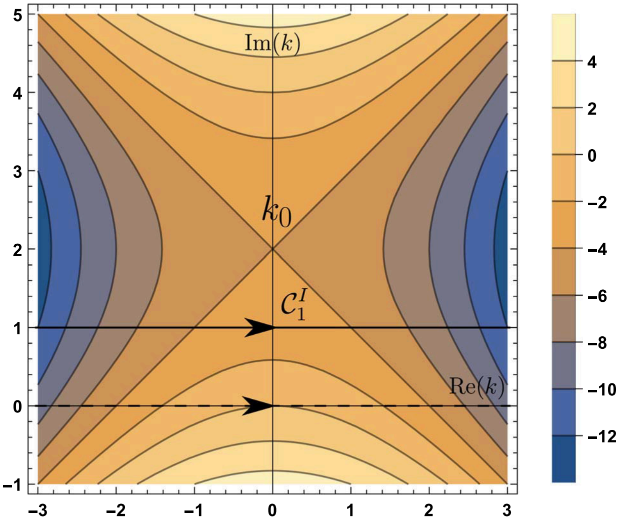

FIG. 4. The deformed horizontal contour $\mathcal{C}_1^I$ (solid) passing through i with $\delta = 1, x = 4, t = 1, k_0 = 2i$. The undeformed contour (dashed). The background contour plot shows the level sets of $\mathrm{Re}(\theta(k,x,t))$. The integrand of I_1 is analytic for $\mathrm{Im}\,(k) < 1$ when $q_0 \in C_1^\infty$.

line $\mathrm{Im}(k) = \delta$ since $t > 0, x > 0$. Hence, the deformed path that we choose is a horizontal line $\mathcal{C}_1^I = \{k \in \mathbb{C} : \mathrm{Im}\,(k) = h\}$, with $h = \min(\delta, x/2t)$.

$$I_1 = -\frac{1}{2\pi}\int_{-\infty}^{\infty} e^{ikx-\omega(k)t}\hat{q}_0(k)\,\mathrm{d}k = -\frac{1}{2\pi}\int_{\mathcal{C}_1^I} e^{ikx-k^2t}\hat{q}_0(k)\,\mathrm{d}k.$$

The contour is shown in Fig. 4. The uniform convergence of Clenshaw–Curtis quadrature applied to I_1 for $x, t \geq c$ is established in Theorem 2 (Appendix), after proper truncation and rescaling.

3.2.2 *I_2: the integral involving $\hat{q}_0(-k)$.* Similar analysis can be applied to I_2 in (7). Here

$$I_2 = -\frac{1}{2\pi}\int_{\partial D^+} e^{ikx-\omega(k)t}\hat{q}_0(-k)\,\mathrm{d}k.$$

Because $\hat{q}_0(-k)$ is analytic and bounded for $\mathrm{Im}(k) > -\delta$, we can deform the contour ∂D^+ to the horizontal line passing through $k_0 = ix/2t$ defined by $\mathcal{C}_2^I = \{k \in \mathbb{C} : \mathrm{Im}\,(k) = x/2t\}$,

$$I_2 = -\frac{1}{2\pi}\int_{\mathcal{C}_2^I} e^{ikx-\omega(k)t}\hat{q}_0(-k)\,\mathrm{d}k.$$

The contour is shown in Fig. 5. The uniform convergence of Clenshaw–Curtis quadrature applied to I_2 for $x, t \geq c$ is established in Theorem 2 (Appendix), after proper truncation and rescaling.

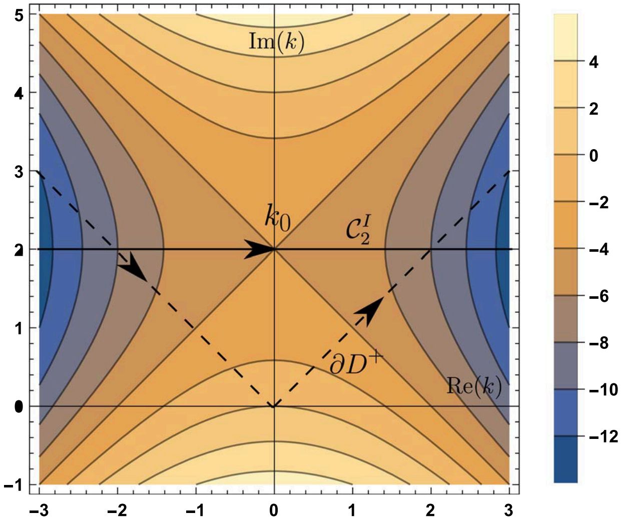

FIG. 5. The deformed horizontal contour for I_2 (solid) through $k_0 = 2i$ with $\delta = 1, x = 4, t = 1$. The undeformed contour (dashed). The background contour plot shows the level sets of $\mathrm{Re}(\theta(k,x,t))$. The integrand of I_2 is analytic for $\mathrm{Im}\,(k) > -1$. The dashed line is the undeformed contour ∂D^+.

3.2.3 B_0: *the integral of the transform of boundary data* $\tilde{g}_0(\omega(k),t)$. The integral B_0 in (7) containing the boundary data is more complicated compared to the integrals I_1, I_2. There are two important factors that require special treatment:

1. The parameter t appears both in the exponential and in the transformed boundary data $\tilde{g}(\omega(k),t)$, and therefore the phase $\theta(k,x,t)$ alone does not describe the decay of the integrand in B_0.
2. The evaluation of $e^{-k^2t}\tilde{g}(\omega(k),t)$ is ill-conditioned due to the oscillations and growth in $\tilde{g}(\omega(k),t)$ cancelling those from the exponential.

Example. To get a more concrete understanding consider $g_0(t) = e^{-t}$. The transform is

$$\tilde{g}_0(\omega(k),t) = \int_0^t e^{k^2 s}e^{-s}\,\mathrm{d}s = \frac{1}{k^2-1}\left(e^{(k^2-1)t} - 1\right).$$

Since $g_0(s) = e^{-s}$ is bounded on the finite interval $0 \le s \le t$, the transformed data $\tilde{g}_0(\omega(k),t)$ are an entire function of k with removable poles at $k = \pm 1$. The integrand of B_0 contains two terms:

$$e^{ikx-\omega(k)t}2ik\tilde{g}_0(\omega(k),t) = \frac{ike^{ikx-t}}{\pi(k^2-1)} - \frac{ike^{ikx-k^2t}}{\pi(k^2-1)}. \tag{12}$$

The second term follows the horizontal direction of steepest descent, but the first term is not exponentially localized on horizontal lines in the complex k-plane. Although the integral of the first term on the ∂D^+ is zero, it is not possible to separate the two terms, in general, for all k.

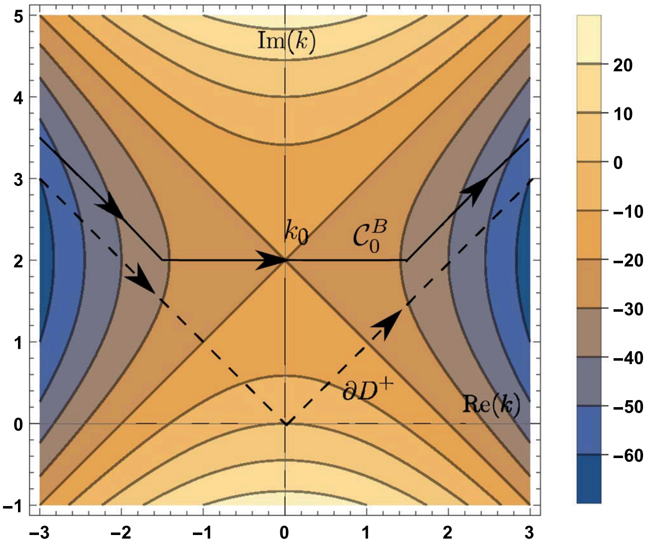

FIG. 6. The undeformed contour ∂D^+. The solid line gives the deformed contour $\mathcal{C}_0^I$ of I_0 that goes through $k_0 = 2i$ and turns to rays parallel to ∂D^+ with $x = 20, t = 5$. The integrand of I_0 is entire. The background contour plot shows the level sets of $\mathrm{Re}(\theta(k, x, t))$.

General case. We write the transform $\tilde{g}_0(k, t)$ as

$$\tilde{g}_0(\omega(k), t) = \int_0^t e^{k^2 s} g_0(s)\,\mathrm{d}s = -\int_t^\infty e^{k^2 s} g_0(s)\,\mathrm{d}s + \int_0^\infty e^{k^2 s} g_0(s)\,\mathrm{d}s,$$

for $k \in D^+$. Therefore, the integrand in B_0 is

$$e^{ikx-k^2t}\tilde{g}_0(\omega(k), t) = -e^{ikx}\int_0^\infty e^{k^2 s} g_0(s+t)\,\mathrm{d}s + e^{ikx-k^2t}\tilde{g}_0(\omega(k), \infty). \tag{13}$$

The two terms on the right-hand side of (13) behave the same as the two terms in (12). Because $\tilde{g}_0(\omega(k), \infty)$ is in general not defined outside D^+ a separation only exists inside D^+. Without splitting the two terms, to get exponential decay for both terms, the contour ∂D^+ is deformed to $\mathcal{C}_0^I$ passing through the saddle point horizontally, and turns up when the second term in the integrand is negligible, see Fig. 6. The corner point $k_1 = \pm L + ix/2t$ is determined by $L = \max(L_1, \sqrt{\gamma})$ with specified tolerance ϵ, where $\left|e^{-L_1^2 t}\right| = \epsilon$ characterizes the exponential decay and $\sqrt{\gamma}$ allows the oblique segment to be away from $k = 0$. With this choice of contour the exponential part in the second term decays exponentially along the horizontal segment, and keeps the same magnitude along the oblique segment while the exponential part in the first term keeps the same magnitude along the horizontal segment, and decays exponentially along the oblique segment. Uniform accuracy is shown in Theorem 3 (Appendix) after proper truncation and rescaling.

REMARK. For boundary data that are not exponentially decaying the transforms $\tilde{g}_0(\omega(k), \infty)$ are only defined in D^+ in Fig. 2. As a result, $\tilde{g}_0(\omega(k), t)$ for large t is highly ill-conditioned when k leaves D^+.

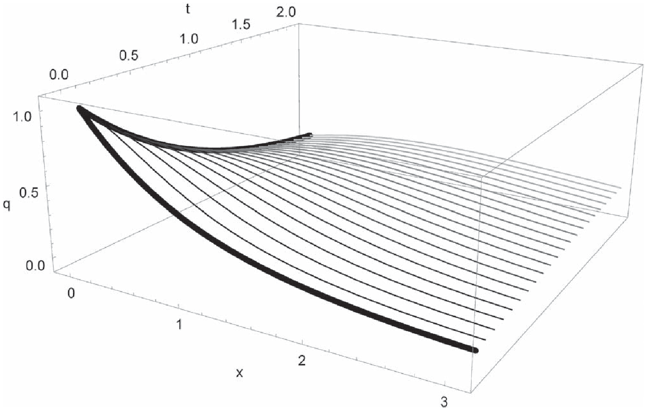

FIG. 7. The solution to the heat equation (6) with exponential decay initial and boundary data $q(x,0) = e^{-x}$, $q(0,t) = e^{-t}$. The bold curves are the initial and boundary conditions.

However, staying inside D^+ requires retaining more oscillations. In the limit $t \to \infty$ the saddle point $x/(2t)$ approaches the corner of D^+, which further restricts contour deformations and makes achieving uniform accuracy more difficult.

3.3 *A numerical example*

With these deformed contours we can numerically evaluate the integrals efficiently for arbitrarily large values of the parameters x, t. Figure 7 shows the solution to the heat equation with initial and boundary data $q_0(x) = e^{-x}$, $g_0(t) = e^{-t}$. Although exact transforms can be obtained for these choices of data, in the rest of the paper, they are only used for computing the errors and our NUTM does not make use of the formulas.

To demonstrate the uniform accuracy for large x, t we plot the absolute errors E_{NUTM} and E_{FCM} along three different curves (a) $t = 0.1$, (b) $x = 0.1$ and (c) $t = x^2$ in Fig. 8. The error E_{NUTM} is obtained using the contours $\mathcal{C}_1^I, \mathcal{C}_2^I$ and $\mathcal{C}_0^B$. The error E_{FCM} is obtained using the contour $\tilde{\mathcal{C}}_0^B$ in (10) Flyer & Fokas (2008). The initial and boundary conditions are $q_0(x) = e^{-10x}$, $g_0(t) = e^{-10t}$ to allow deformation in a larger region. The number of collocation points $N = 120$ is the same for both methods. This is a coarse grid for the integrals with the errors approximately 10^{-3} when $s = 0.1$ is small, but it shows the efficiency of the NUTM as s grows. The true solution is computed using Mathematica's built-in numerical integration routine NIntegrate along the undeformed contour ∂D^+ with sufficient recursions and precision. This is time consuming if the transforms of the initial and boundary data need to be computed. The truncation tolerance is set to 10^{-13} for determining the truncation of the deformed path. This value of the truncation tolerance is chosen so that it is small enough to show the trend of the errors when x, t vary and the truncation is not affected by the rounding errors. These settings are the same for other examples in the paper unless stated otherwise.

The absolute error E_{NUTM} decreases in all cases as x, t grow while E_{FCM} grows when t increases. This can be explained simply by the fact that the contour used in the FCM does not follow the steepest descent path. Furthermore, even when t is fixed in Fig. 8(a), E_{FCM} decreases slower than E_{NUTM}. On the other hand, E_{NUTM} increases relative to the true solution. This is mainly due to the fact that the magnitude of the solution is smaller than the truncation tolerance for $x > 5$, at which point the numerical

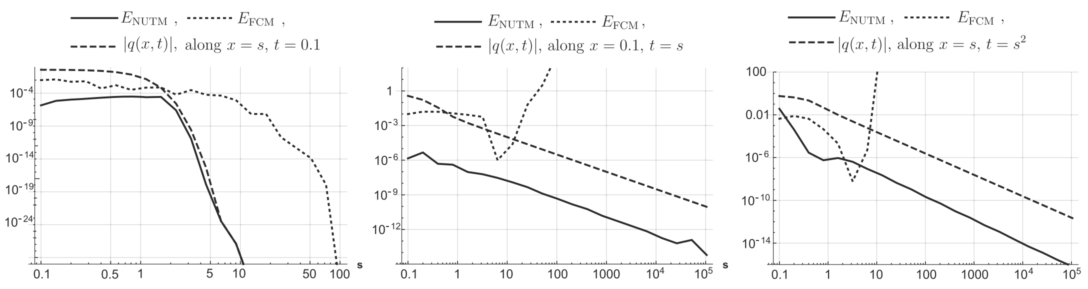

(a) (b) (c)

Fig. 8. The absolute errors of the numerical solution to the heat equation with initial condition $q_0(x) = e^{-10x}$ and boundary condition $g_0(t) = e^{-10t}$ along (a) $x = s, t = 0.1$, (b) $x = 0.1, t = s$, (c) $x = s, t = s^2$ for $s \in [0.1, 10^5]$. The error E_{NUTM} is obtained using the contours $\mathcal{C}_1^I, \mathcal{C}_2^I$ and $\mathcal{C}_0^B$. The error E_{FCM} is obtained using the contour $\tilde{\mathcal{C}}_0^B$ in Fig. 6. The absolute value of the solution $|q(x,t)|$ is also plotted with dashed lines for reference. The FCM loses accuracy as t grows while E_{NUTM} decreases in all cases as parameters increase.

solution has almost all contours truncated. In Fig. 8(b–c), E_{NUTM} maintains good relative accuracy. In Fig. 8(c), E_{NUTM} starts with a larger error, because $t = s^2 = 0.01$ is very small and close to the initial condition, which requires more nodes to produce the same order of errors compared with the other two starting from $t = 0.1$. As both the FCM and the NUTM are implemented with spectral methods, for fixed x and t, both methods are spectrally accurate.

Remark. As can be seen in (12) and (13), there is large cancellation in the exponentials. To avoid potential overflow/underflow problems we use $\hat{g}_0(\omega(k), T)$ defined by

$$\hat{g}_0(\omega(k), T) = e^{-\omega(k)T}\tilde{g}_0(\omega(k), T) = \int_0^T e^{\omega(k)(s-T)} g_0(s)\,\mathrm{d}s. \tag{14}$$

4. The LS equation on the half-line

Next, we consider a dispersive example, the LS equation:

$$iq_t = -q_{xx}, \quad x > 0, \ t > 0, \tag{15}$$

with Dirichlet boundary data $g_0 \in C_\gamma^\infty$ and initial data $q_0 \in C_\delta^\infty$.

4.1 *The solution formula from the UTM*

The dispersion relation for (15) is $\omega(k) = ik^2$. Define the transform of the initial data $\hat{q}_0$ and the transform of the Dirichlet boundary data $\tilde{g}_0$ by (2) and (4). The UTM provides the solution in terms of the following contour integrals (Deconinck *et al.*, 2014),

$$q(x,t) = \frac{1}{2\pi}\int_{-\infty}^{\infty} e^{ikx-\omega(k)t}\hat{q}_0(k)\,\mathrm{d}k - \frac{1}{2\pi}\int_{\partial D^+} e^{ikx-\omega(k)t}\left[\hat{q}_0(-k) - 2k\tilde{g}_0(\omega(k), t)\right]\mathrm{d}k, \tag{16}$$

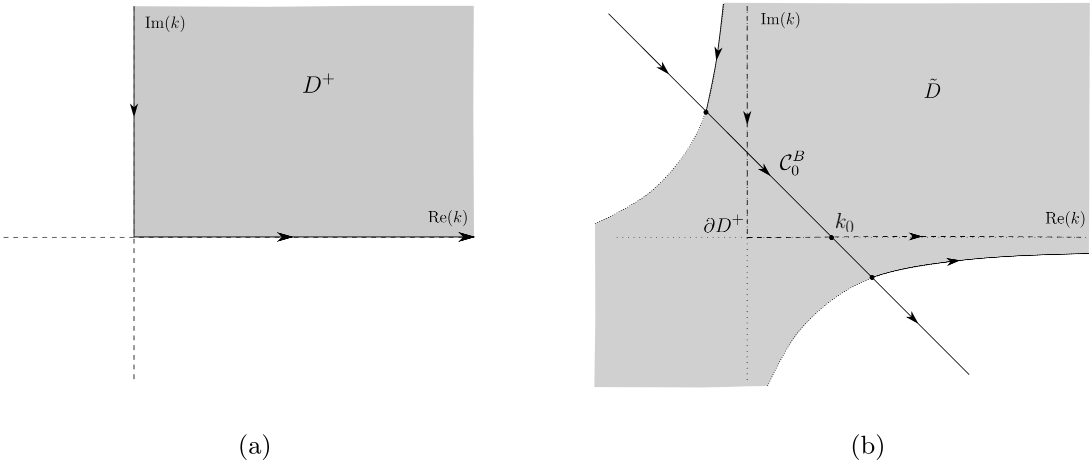

FIG. 9. Regions for the LS equation. Panel (a) shows the region $D^+ = \{k \in \mathbb{C}^+ : \mathrm{Re}(k^2) < 0\}$. Panel (b) shows $\tilde{D} = \{k \in \mathbb{C} : \mathrm{Re}(k^2) < \gamma\}$ and a schematic of the deformed contour from ∂D^+ to $\mathcal{C}_0^B$ for B_0 in (17), see Section 4.2.3 for details of the deformation.

where the contour ∂D^+ is the positively oriented boundary of the first quadrant $D^+ = \{k \in \mathbb{C} : \mathrm{Re}\,(k) \geq 0, \mathrm{Im}\,(k) \geq 0\}$. With the assumption of the decay of $g_0(t)$ the contour can be deformed to the lower-half plane inside $\tilde{D} = \{k \in \mathbb{C} : \mathrm{Re}\left(k^2\right) < \gamma\}$ as in Fig. 9. However, this is not enough to completely eliminate the oscillations. In general, other methods for oscillatory integrals are required when t is not sufficiently large or the saddle point k_0 has large modulus.

4.2 *Deformations of the contours based on the method of steepest descent*

We separate the different integrals in the solution formula (16)

$$q(x,t) = I_0 + I_1 + B_0, \tag{17}$$

where

$$\begin{aligned} I_0 &= \frac{1}{2\pi}\int_{-\infty}^{\infty} e^{ikx-\omega(k)t}\hat{q}_0(k)\,\mathrm{d}k,\\ I_1 &= -\frac{1}{2\pi}\int_{\partial D^+} e^{ikx-\omega(k)t}\hat{q}_0(-k)\,\mathrm{d}k,\\ B_0 &= \frac{1}{2\pi}\int_{\partial D^+} e^{ikx-\omega(k)t}2k\tilde{g}_0(\omega(k),t)\,\mathrm{d}k. \end{aligned}$$

4.2.1 I_1: *integral with the transform of the initial data.* The phase function in I_1 is

$$\theta(k;x,t) = ikx - \omega(k)t = ikx - ik^2t. \tag{18}$$

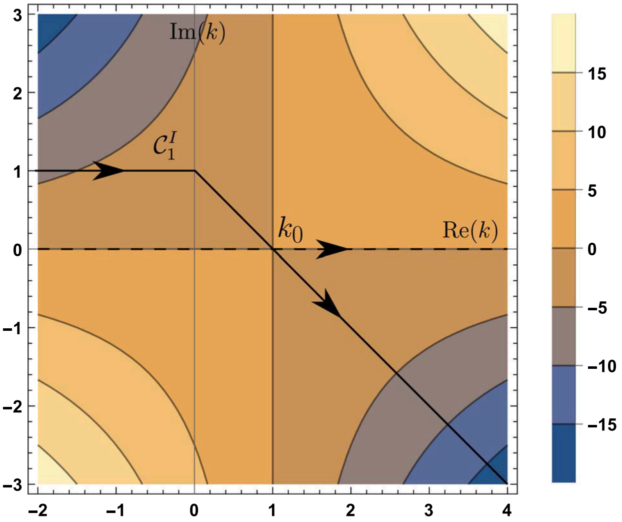

FIG. 10. The undeformed contour (dashed). The deformed horizontal contour $\mathcal{C}_1^I$ (solid) going through $k_0 = 1, \delta = 1, x = 2, t = 1$. The background contour plot shows the level sets of $\mathrm{Re}(\theta(k, x, t))$. The integrand of I_1 is analytic for $\mathrm{Im}\,(k) < 1$.

There is one saddle point $k_0 = x/2t$ on the positive real axis satisfying $\theta'(k_0; x, t) = 0$. Near the saddle point k_0,

$$\theta(k; x, t) = ikx - ik^2t = -it(k - x/2t)^2 + ix^2/4t.$$

The directions of steepest descent are $-\pi/4$ and $3\pi/4$. Similar to the case of the heat equation, the transformed initial data $\hat{q}_0(k)$ are bounded and analytic in $\mathrm{Im}\,(k) < \delta$ when $q_0 \in C_\delta^\infty$. Hence, we choose the deformed contour $\mathcal{C}_1^I = \{a + k_0 + ib : a \in (-\infty, -\delta), b = \delta\} \cup \{a + k_0 - ia : a \in [-\delta, \infty)\}$ to be a horizontal ray with height $\mathrm{Im}(k) = \delta$, and a straight-line segment with slope -1 passing through the saddle point as shown in Fig. 10. The integral I_1 becomes

$$I_1 = \frac{1}{2\pi} \int_{\mathcal{C}_1^I} e^{ikx - ik^2t} \hat{q}_0(k)\, \mathrm{d}k.$$

4.2.2 *I_2: integral with the transform of the initial data $\hat{q}_0(-k)$.* Similar analysis can be applied to I_2 with $\hat{q}_0(-k)$ in (16). Since the transform $\hat{q}_0(-k)$ is analytic and bounded for $\mathrm{Im}\,(k) > -\delta$, we can deform the contour ∂D^+ to

$$\mathcal{C}_2^I = \{a + k_0 - ia : a \in (-\infty, \delta)\} \cup \{a + k_0 - ib : a \in [\delta, \infty), b = \delta\},$$

see Fig. 11. Therefore, I_2 becomes

$$I_2 = -\frac{1}{2\pi} \int_{\mathcal{C}_2^I} e^{ikx - ik^2t} \hat{q}_0(-k)\, \mathrm{d}k.$$

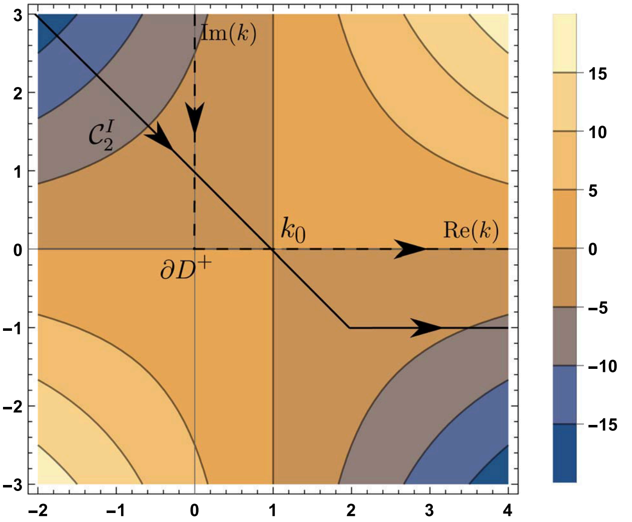

FIG. 11. The undeformed contour (dashed). The deformed contour for I_2 (solid) going through $k_0 = 1, \delta = 1, x = 2, t = 1$. The background contour plot shows the level sets of $\mathrm{Re}(\theta(k, x, t))$. The integrand of I_2 is analytic for $\mathrm{Im}\,(k) > -1$.

4.2.3 B_0: *integral of the transform of boundary data* $\tilde{g}_0(\omega(k), t)$. The issues discussed in Section 3.2.3 also appear in the case of the LS equation. However, now the region where we can deform the contour is restricted. The same decomposition as in (13) gives

$$e^{ikx-k^2t}\tilde{g}_0(\omega(k), t) = -e^{ikx}\int_0^\infty e^{k^2s}g_0(s+t)\,\mathrm{d}s + e^{ikx-k^2t}\tilde{g}_0(\omega(k), \infty). \tag{19}$$

For generic $g_0(t)$, if the contour of B_0 is along the $-\pi/4$ direction at the saddle point $k_0 = x/2t$, the first term in (19) grows exponentially as $x \to \infty$ since $\mathrm{Re}\,(ikx) > 0$. On the other hand, $\tilde{g}_0(\omega(k), \infty)$ may not be extendable outside D^+. With the assumption that $g_0 \in C_\gamma^\infty$ it becomes possible to deform the path to the lower-half plane to obtain some exponential decay. The steps of the deformation are the following:

1. The region D^+ is extended to $\tilde{D}$. The transformed data $\tilde{g}_0(\omega(k), \infty)$ are analytic in $\tilde{D}$ and continuous up to $\partial\tilde{D}$.
2. The contour ∂D^+ is deformed to $\mathcal{C}_{0,a}^B \cup \mathcal{C}_{0,b}^B \cup \mathcal{C}_{0,c}^B$ as shown in Fig. 12, where $\mathcal{C}_{0,b}^B$ is the straight-line segment passing through the saddle point along the steepest-descent direction up to $\partial\tilde{D}$, and $\mathcal{C}_{0,a}^B, \mathcal{C}_{0,c}^B$ are the unbounded curved segments along $\partial\tilde{D}$.
3. Using that $e^{ikx-\omega(k)t}\int_t^\infty e^{\omega(k)s}g_0(s)\,\mathrm{d}s$ is bounded and analytic in $\tilde{D}$, we can replace $\tilde{g}_0(\omega(k), t)$ with $\tilde{g}_0(\omega(k), \infty)$ using Jordan's lemma,

$$B_0 = \frac{1}{2\pi}\int_{\partial D^+} e^{ikx-\omega(k)t}2k\tilde{g}_0(\omega(k), t)\,\mathrm{d}k = \frac{1}{2\pi}\int_{\mathcal{C}_{0,a}^B\cup\mathcal{C}_{0,b}^B\cup\mathcal{C}_{0,c}^B} e^{ikx-\omega(k)t}2k\tilde{g}_0(\omega(k), \infty)\,\mathrm{d}k. \tag{20}$$

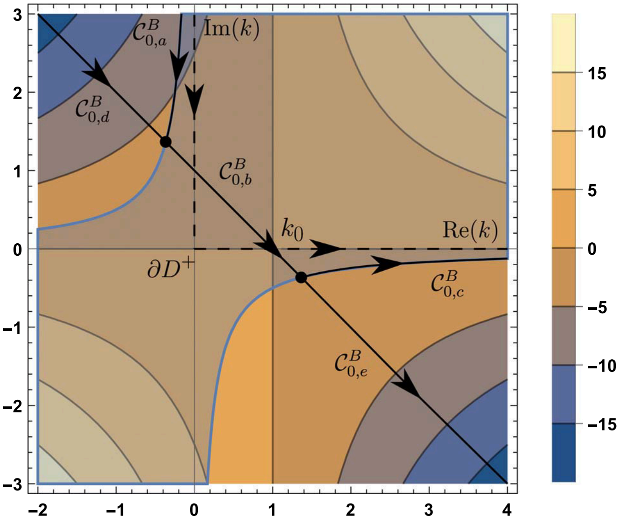

FIG. 12. The undeformed contour (dashed). The deformed contour for B_0 (solid) through $k_0 = 1$ with $x = 2, t = 1, \gamma = 1$, see Section 4.2.3 for details of the deformation. The background contour plot shows the level sets of $\mathrm{Re}(\theta(k,x,t))$.

4. The integral along $\mathcal{C}^B_{0,a}$ is decomposed into two parts to maximize decay along the steepest descent direction:

$$\int_{\mathcal{C}^B_{0,a}} e^{ikx-\omega(k)t} 2k\tilde{g}_0(\omega(k),\infty)\,\mathrm{d}k = \int_{\mathcal{C}^B_{0,d}} e^{ikx-\omega(k)t} 2k\tilde{g}_0(\omega(k),t)\,\mathrm{d}k + \int_{\mathcal{C}^B_{0,a}} e^{ikx-\omega(k)t} 2k\tilde{g}^c_0(\omega(k),t)\,\mathrm{d}k,$$

where

$$\tilde{g}^c_0(\omega(k),t) = \int_t^\infty e^{\omega k s} g_0(s)\,\mathrm{d}s,$$

is the complementary transform of g_0.

5. The integral along $\mathcal{C}^B_{0,c}$ is decomposed into two parts:

$$\begin{aligned}\int_{\mathcal{C}^B_{0,c}} e^{ikx-\omega(k)t} 2k\tilde{g}_0(\omega(k),\infty)\,\mathrm{d}k &= \int_{\mathcal{C}^B_{0,c}} e^{ikx-\omega(k)t} 2\left(k\tilde{g}_0(\omega(k),\infty) - k_0\tilde{g}_0(\omega(k_0),\infty)\right)\,\mathrm{d}k \\ &\quad + \int_{\mathcal{C}^B_{0,e}} e^{ikx-\omega(k)t} 2k_0\tilde{g}_0(\omega(k_0),\infty)\,\mathrm{d}k.\end{aligned}$$

The second integral on the right-hand side is deformed to follow the direction of steepest descent.

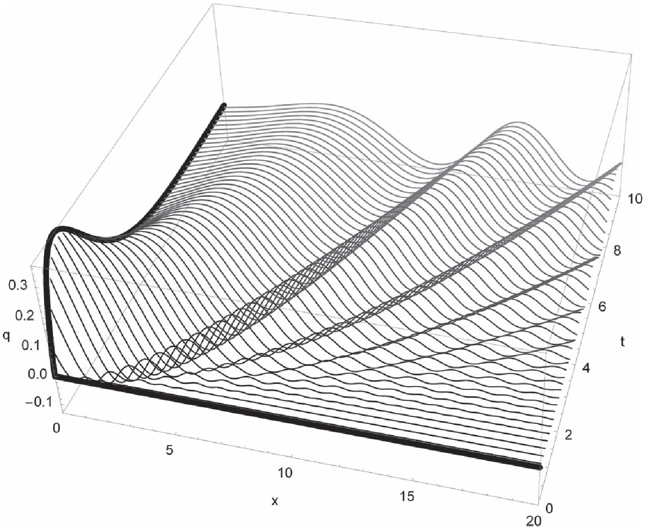

FIG. 13. The plot of the real part of the solution of the LS equation with $q_0(x) = 0$, $g_0(t) = te^{-t}$. The bold solid curve shows the initial and boundary conditions.

6. With the above steps we obtain

$$\begin{aligned} B_0 =& \frac{1}{2\pi}\int_{\mathcal{C}^B_{0,a}} e^{ikx-\omega(k)t} 2k\tilde{g}^c_0(\omega(k),t)\,\mathrm{d}k + \frac{1}{2\pi}\int_{\mathcal{C}^B_{0,d}} e^{ikx-\omega(k)t} 2k\tilde{g}_0(\omega(k),t)\,\mathrm{d}k \\ &+ \frac{1}{2\pi}\int_{\mathcal{C}^B_{0,b}} e^{ikx-\omega(k)t} 2k\tilde{g}_0(\omega(k),\infty)\,\mathrm{d}k \\ &+ \frac{1}{2\pi}\int_{\mathcal{C}^B_{0,c}} e^{ikx-\omega(k)t} \left[2k\tilde{g}_0(\omega(k),\infty) - 2k_0\tilde{g}_0(\omega(k_0),\infty)\right]\,\mathrm{d}k \\ &+ \frac{1}{2\pi}\int_{\mathcal{C}^B_{0,e}} e^{ikx-\omega(k)t} 2k_0\tilde{g}_0(\omega(k_0),\infty)\,\mathrm{d}k. \end{aligned}$$

Using the deformed contour, for large x, t, the integral is exponentially localized near the saddle point on $\mathcal{C}^B_{0,b}$. When the integrand is not sufficiently small near the endpoints of $\mathcal{C}^B_{0,b}$, the oscillations in the integrand along $\mathcal{C}^B_{0,c}$ and $\mathcal{C}^B_{0,d}$ become important. Most of the potential error comes from the integral along $\mathcal{C}^B_{0,c}$, as the integrand along $\mathcal{C}^B_{0,d}$ has exponential decay from the e^{ikx} factor. The contour $\mathcal{C}^B_{0,c}$ asymptotically approaches the real axis. We use the Levin collocation method (Iserles *et al.*, 2006) for the integrals along $\mathcal{C}^B_{0,c}$ and $\mathcal{C}^B_{0,d}$ to maintain accuracy for large x, t. The rest of the integrals in B_0, as well as those making up I_1 and I_2, are computed using Clenshaw–Curtis quadrature.

4.3 *A numerical example*

Consider the initial condition $q_0(x) = 0$, and the Dirichlet boundary condition $g_0(t) = te^{-t}$. The real part of the solution to (15) with this choice of data is shown in Fig. 13. Dispersive waves quickly emerge from the boundary, becoming more oscillatory for large x. The absolute error and the magnitude of the solution evaluated along (a) $t = 0.1$, (b) $x = 0.1$, (c) $t = x^2$ are shown in Fig. 14. The errors shown in

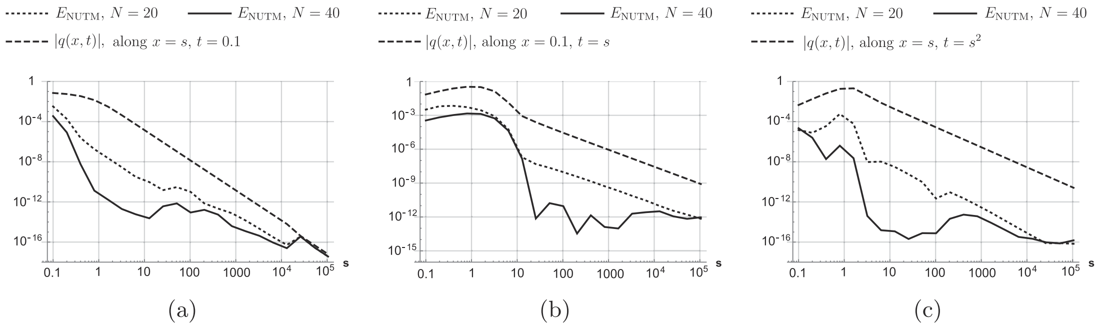

(a) (b) (c)

Fig. 14. The absolute errors E_{NUTM} of the numerical solution to the LS equation (15) along three curves: (a) $x = s, t = 0.1$, (b) $x = 0.1, t = s$, (c) $x = s, t = s^2$ for $s \in [0.1, 10^5]$.

dotted curves are computed with $N = 20$ collocation points for each part of the contour in B_0, while the errors shown in solid curves are computed with $N = 40$ collocation points. The absolute errors decrease as x, t increase. In Fig. 14(a), we see that although the initial condition is zero, at $t = 0.1$ the solution $q(x, t)$ only decreases algebraically. This makes traditional time-stepping method inefficient even if we ignore issues related to the highly oscillatory nature of the solution.

5. A multi-term third-order PDE

The deformations for higher-order equations are more involved and the integrands may have branch points that are fixed by the equation, and not by the initial or boundary data. The NUTM is implemented in a systematic way, as long as one can solve the PDE using the UTM with additional care for the branch points. Consider a multi-term third-order PDE,

$$q_t = q_x + q_{xxx}, \quad x > 0,\ t > 0, \tag{21}$$

with Dirichlet boundary data $g_0 \in C_\gamma^\infty$, Neumann boundary data $g_1 \in C_\gamma^\infty$ and initial data $q_0 \in C_\delta^\infty$. The dispersion relation is $\omega(k) = -ik + ik^3$ and $D^+ = \{k \in \mathbb{C}^+ : \operatorname{Re}(\omega(k)) < 0\} = D_1^+ \cup D_2^+$ as shown in Fig. 15.

Using the UTM it is known that the problem requires two boundary conditions at $x = 0$ (Deconinck *et al.*, 2014). By solving $\omega(\nu(k)) = \omega(k)$ we find two symmetries of the dispersion relation,

$$\nu_1(k) = (-k - \sqrt{4 - 3k^2})/2,$$
$$\nu_2(k) = (-k + \sqrt{4 - 3k^2})/2,$$

with branch cut $[-2/\sqrt{3}, 2/\sqrt{3}]$. Here, ν_1 is the branch of ν that tends to $(-1/2 + i\sqrt{3}/2)k = k\exp(2\pi i/3)$ as $k \to \infty$ and ν_2 is the other branch. The solution formula is given by[3]

$$q(x, t) = I_1 + I_2 + I_3 + B_0 + B_1, \tag{22}$$

---

[3] Although some parts of the contours lie on the branch cut the integrands are well defined if the values are taken as limits from the interior of D^+.

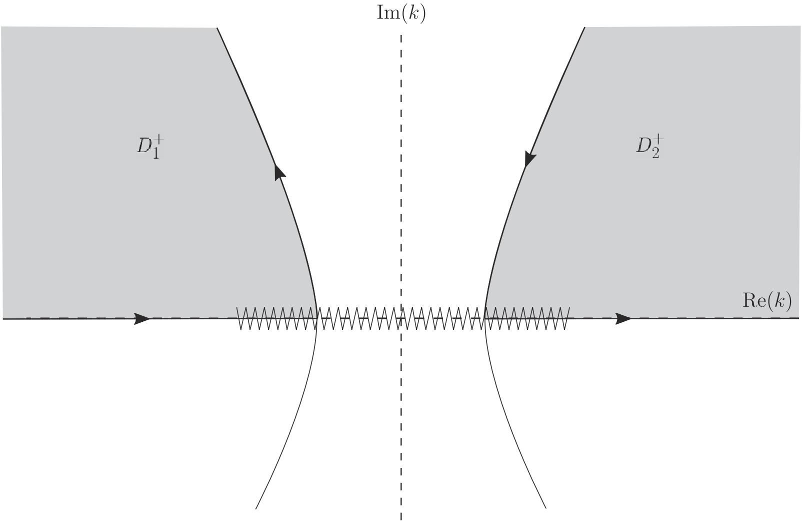

FIG. 15. The region D^+ for (21). The shaded region in the top left is D_1^+. The shaded region in the top right is D_2^+. The branch cut is shown as a jagged line.

with

$$I_1 = \frac{1}{2\pi}\int_{-\infty}^{\infty} e^{ikx-\omega(k)t}\hat{q}_0(k)\,\mathrm{d}k,$$
$$I_2 = -\frac{1}{2\pi}\int_{\partial D_1^+} e^{ikx-\omega(k)t}\hat{q}_0(\nu_1(k))\,\mathrm{d}k,$$
$$I_3 = -\frac{1}{2\pi}\int_{\partial D_2^+} e^{ikx-\omega(k)t}\hat{q}_0(\nu_2(k))\,\mathrm{d}k,$$

$$B_0 = -\frac{1}{2\pi}\int_{\partial D_1^+} e^{ikx-\omega(k)t}(\nu_1^2(k)-k^2)\tilde{g}_0(\omega(k),t)\,\mathrm{d}k - \frac{1}{2\pi}\int_{\partial D_2^+} e^{ikx-\omega(k)t}(\nu_2^2(k)-k^2)\tilde{g}_0(\omega(k),t)\,\mathrm{d}k,$$
$$B_1 = -\frac{1}{2\pi}\int_{\partial D_1^+} e^{ikx-\omega(k)t}(ik-i\nu_1(k))\tilde{g}_1(\omega(k),t)\,\mathrm{d}k - \frac{1}{2\pi}\int_{\partial D_2^+} e^{ikx-\omega(k)t}(ik-i\nu_2(k))\tilde{g}_1(\omega(k),t)\,\mathrm{d}k.$$

For convenience, we impose the following initial and boundary conditions to focus on the deformation of B_0,

$$q(x,0)=0,\ q(0,t)=g_0(t),\ g_0\in C_\gamma^\infty,\ q_x(0,t)=0.$$

For inhomogeneous initial and Neumann data the deformation of B_1 follows the same steps as the deformation of B_0, and the deformations of I_1, I_2, I_3 follow the same steps as in I_1, I_2 in the heat equation or the LS equation case.

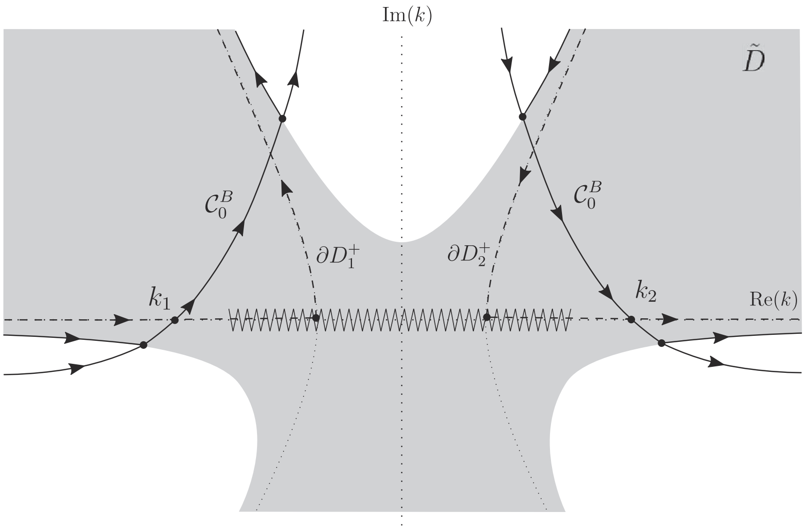

FIG. 16. The region $\tilde{D}$ and the deformation for B_0 across the saddle points k_1 and k_2. The branch cut is shown as a jagged line.

5.1 *Deformations of the contour of B_0 based on the method of steepest descent*

With homogeneous initial and Neumann boundary conditions, the solution reduces to

$$q(x,t) = B_0 = B_0|_{D_1^+} + B_0|_{D_2^+},$$

where

$$B_0|_{D_1^+} = -\frac{1}{2\pi}\int_{\partial D_1^+} e^{ikx-\omega(k)t}(\nu_1^2(k) - k^2)\tilde{g}_0(\omega(k),t)\,\mathrm{d}k,$$
$$B_0|_{D_2^+} = -\frac{1}{2\pi}\int_{\partial D_2^+} e^{ikx-\omega(k)t}(\nu_2^2(k) - k^2)\tilde{g}_0(\omega(k),t)\,\mathrm{d}k.$$

The phase function in B_0 is

$$\theta(k;x,t) = ikx - \omega(k)t = ikx - (-ik + ik^3)t.$$

There are two saddle points $k_{1,2} = \pm\sqrt{x/(3t) + 1/3}$ on the real axis satisfying $\theta'(k;x,t) = 0$, $k_1 \in D_1^+$ and $k_2 \in D_2^+$. Since the saddle points and contours are symmetric with respect to the imaginary axis, we only need to analyse the deformation for D_2^+ and use the mirror image about the imaginary axis for D_1^+. Near the saddle point k_2, θ has the expansion

$$\theta(k;x,t) = \frac{2}{9}i\left(t\sqrt{\frac{3(t+x)}{t}} + x\sqrt{\frac{3(t+x)}{t}}\right) - it\sqrt{\frac{3(t+x)}{t}}(k-k_2)^2 + \mathcal{O}(k-k_2)^3.$$

The direction of steepest descent is along the angles $-\pi/4$ and $3\pi/4$. The integrands need to be extended to the lower half plane similar to the steps in Section 4.2.3. A sketch of the deformation of the contour is shown in Fig. 16.

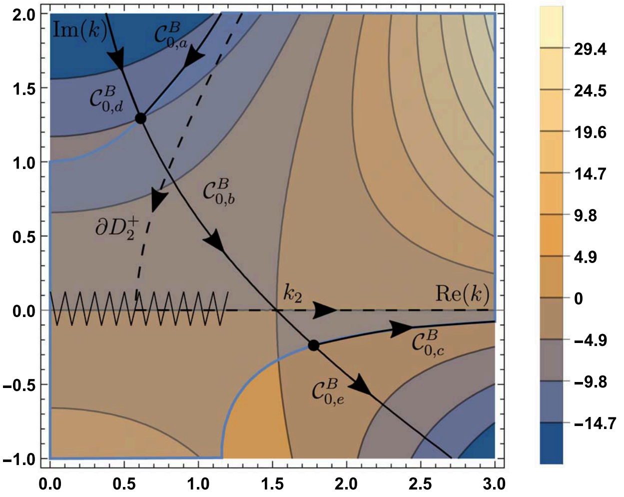

FIG. 17. The deformed contour for $B_0|_{D_2}$ when $x \geq 3t$ (solid), the undeformed contour (dashed). The background contour plot shows the level sets of $\mathrm{Re}(\theta(k,x,t))$. The branch cut is shown as a jagged line.

5.1.1 *Deformations of the contour of B_0 for $x \geq 3t$.* In this case the saddle points k_1,k_2 lie outside branch cut $[-2/\sqrt{3}, 2\sqrt{3}]$. We proceed as follows:

1. The region $D^+ = \{k \in \mathbb{C}^+ : \mathrm{Re}\,(\omega(k)) < 0\}$ is extended to $\tilde{D} = \{k \in \mathbb{C} : \mathrm{Re}\,(\omega(k)) < \gamma\}$. The transformed data $\tilde{g}_0(\omega(k), \infty)$ are analytic in $\tilde{D}$ and continuous up to $\partial\tilde{D}$.

2. The contour ∂D^+ is deformed to $\mathcal{C}^B_{0,a} \cup \mathcal{C}^B_{0,b} \cup \mathcal{C}^B_{0,c}$ as shown in Fig. 17. $\mathcal{C}^B_{0,b}$ is the curve passing through the saddle point up to $\partial\tilde{D}$, keeping $\mathrm{Im}\,(\theta(k;x,t))$ constant along the steepest-descent direction and $\mathcal{C}^B_{0,a}, \mathcal{C}^B_{0,c}$ are the unbounded curve segments along $\partial\tilde{D}$.

3. Using that $e^{ikx-\omega(k)t}\int_t^\infty e^{\omega(k)s} g_0(s)\,\mathrm{d}s$ is bounded and analytic in $\tilde{D}$, we can replace $\tilde{g}_0(\omega(k), t)$ with $\tilde{g}_0(\omega(k), \infty)$,

$$\begin{aligned} B_0|_{D_2^+} =& \frac{1}{2\pi}\int_{\partial D_2^+} e^{ikx-\omega(k)t}(\nu_2^2(k) - k^2)\tilde{g}_0(\omega(k), t)\,\mathrm{d}k \\ =& \frac{1}{2\pi}\int_{\mathcal{C}^B_{0,a}\cup\mathcal{C}^B_{0,b}\cup\mathcal{C}^B_{0,c}} e^{ikx-\omega(k)t}(\nu_2^2(k) - k^2)\tilde{g}_0(\omega(k), \infty)\,\mathrm{d}k. \end{aligned}$$

4. The integral along $\mathcal{C}^B_{0,a}$ is decomposed into two parts to maximize decay along the steepest-descent direction:

$$\int_{\mathcal{C}^B_{0,a}} e^{ikx-\omega(k)t}(\nu_2^2(k) - k^2)\tilde{g}_0(\omega(k), \infty)\,\mathrm{d}k =$$
$$\int_{\mathcal{C}^B_{0,a}} e^{ikx-\omega(k)t}(\nu_2^2(k) - k^2)\tilde{g}_0^c(\omega(k), t)\,\mathrm{d}k + \int_{\mathcal{C}^B_{0,d}} e^{ikx-\omega(k)t}(\nu_2^2(k) - k^2)\tilde{g}_0(\omega(k), t)\,\mathrm{d}k,$$

where

$$\tilde{g}_0^c(\omega(k),t) = \int_t^{\infty} e^{\omega(k)s} g_0(s)\,\mathrm{d}s,$$

is the complement of the transform $\tilde{g}_0(\omega(k),t)$ and $\mathcal{C}^B_{0,d}$ is extended from $\mathcal{C}^B_{0,b}$, keeping $\mathrm{Im}\,(\theta(k;x,t))$ constant along the steepest-descent direction.

5. The integral along $\mathcal{C}^B_{0,c}$ is decomposed into two parts to separate the leading-order contribution in the oscillatory integral:

$$\int_{\mathcal{C}^B_{0,c}} e^{ikx-\omega(k)t}(\nu_2^2(k)-k^2)\tilde{g}_0(\omega(k),\infty)\,\mathrm{d}k = \int_{\mathcal{C}^I_{0,e}} e^{ikx-\omega(k)t}(\nu_2^2(k_2)-k_2^2)\tilde{g}_0(\omega(k_2),\infty)\,\mathrm{d}k$$
$$+\int_{\mathcal{C}^B_{0,c}} e^{ikx-\omega(k)t}\Big[(\nu_2^2(k)-k^2)\tilde{g}_0(\omega(k),\infty)-(\nu_2^2(k_2)-k_2^2)\tilde{g}_0(\omega(k_2),\infty)\Big]\,\mathrm{d}k.$$

The contour $\mathcal{C}^B_{0,e}$ is extended from $\mathcal{C}^B_{0,b}$, keeping $\mathrm{Im}\,(\theta(k;x,t))$ constant along the steepest-descent direction.

6. Finally, we obtain

$$B_0|_{D_2^+} = \frac{1}{2\pi}\int_{\mathcal{C}^I_{0,a}} e^{ikx-\omega(k)t}(\nu_2^2(k)-k^2)\tilde{g}_0^c(\omega(k),t)\,\mathrm{d}k + \frac{1}{2\pi}\int_{\mathcal{C}^B_{0,d}} e^{ikx-\omega(k)t}(\nu_2^2(k)-k^2)\tilde{g}_0(\omega(k),t)\,\mathrm{d}k$$
$$+\frac{1}{2\pi}\int_{\mathcal{C}^B_{0,b}} e^{ikx-\omega(k)t}(\nu_2^2(k)-k^2)\tilde{g}_0(\omega(k),\infty)\,\mathrm{d}k$$
$$+\frac{1}{2\pi}\int_{\mathcal{C}^B_{0,c}} e^{ikx-\omega(k)t}(\nu_2^2(k)-k^2)\tilde{g}_0(\omega(k),\infty)-(\nu_2^2(k_2)-k_2^2)\tilde{g}_0(\omega(k_2),\infty)\,\mathrm{d}k$$
$$+\frac{1}{2\pi}\int_{\mathcal{C}^B_{0,e}} e^{ikx-\omega(k)t}(\nu_2^2(k_2)-k_2^2)\tilde{g}_0(\omega(k_2),\infty)\,\mathrm{d}k.$$

The integrals along $\mathcal{C}^B_{0,b}, \mathcal{C}^B_{0,d}$ and $\mathcal{C}^B_{0,e}$ are computed using Clenshaw–Curtis quadrature, and the integrals along $\mathcal{C}^B_{0,a}$ and $\mathcal{C}^B_{0,c}$ are computed using Levin's method.

The contour integral $B_0|_{D_1^+}$ is deformed in a symmetrical way. For real-valued data we can use the symmetry and compute $q(x,t)$ with only the contour integral $B_0|_{D_2^+}$,

$$q(x,t) = 2\mathrm{Re}\left(B_0|_{D_2^+}\right).$$

5.1.2 *Deformations of the contour for $B_0|_{D_2^+}$ for $x < 3t$.*

When $x < 3t$ the saddle points k_1, k_2 lie on branch cut $[-2/\sqrt{3}, 2/\sqrt{3}]$. To maximize the use of the steepest-decent direction we choose a different branch cut for ν, shown in Fig. 18 in red. The new branch cut starts from the branch point $2/\sqrt{3}$ and

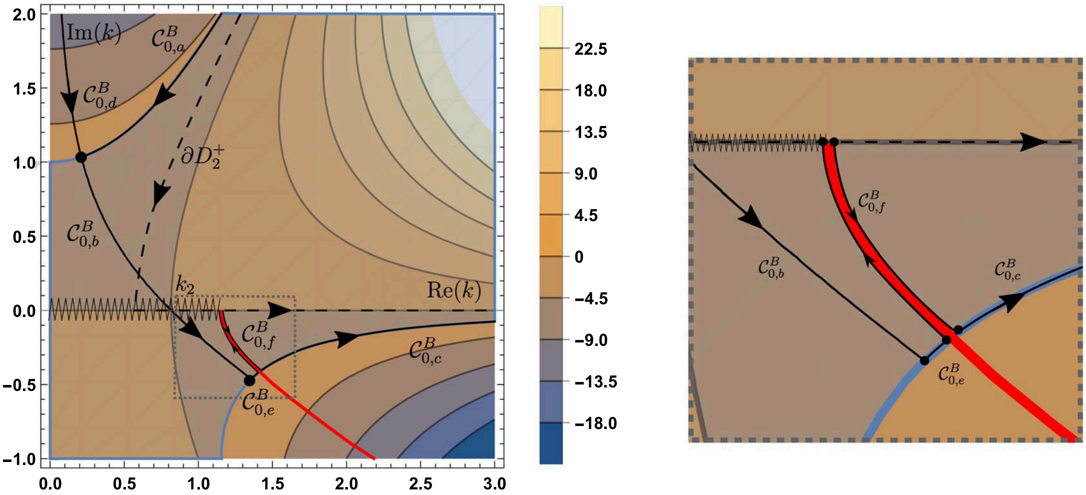

FIG. 18. The deformed contour for $B_0|_{D_2}$ when $x < 3t$ (solid). The undeformed contour (dashed). The background contour plot shows the level sets of $\mathrm{Re}(\theta(k, x, t))$. The original branch cut is shown as a jagged line and the new branch cut is shown in red. A zoomed plot of the contour near the new branch cut is shown in the right panel.

goes along the curve with $\mathrm{Im}\,(\theta(k; x, t))$ constant in the lower half plane. The corresponding $\tilde{\nu}_2(k)$ is defined as the analytic continuation of $\nu_2(k)$ from the interior of D_2^+. We use the following steps:

1. The region $D^+ = \{k \in \mathbb{C}^+ : \mathrm{Re}\,(\omega(k)) < 0\}$ is extended to $\tilde{D} = \{k \in \mathbb{C} : \mathrm{Re}\,(\omega(k)) < \gamma\}$. The transformed data $\tilde{g}_0(\omega(k), \infty)$ are analytic in $\tilde{D}$ and continuous up to $\partial\tilde{D}$.
2. The contour ∂D_2^+ is deformed to $\mathcal{C}^B_{0,a} \cup \mathcal{C}^B_{0,b} \cup \mathcal{C}^B_{0,e} \cup (-\mathcal{C}^B_{0,f}) \cup \mathcal{C}^B_{0,f} \cup \mathcal{C}^B_{0,c}$ as shown in Fig. 18. The contour $\mathcal{C}^B_{0,b}$ is the curve passing through the saddle point up to $\partial\tilde{D}$ with $\mathrm{Im}\,(\theta(k; x, t))$ constant along the steepest-descent direction. The contours $\mathcal{C}^B_{0,a}$, $\mathcal{C}^B_{0,e}$ and $\mathcal{C}^B_{0,c}$ are along $\partial\tilde{D}$. The contours $-\mathcal{C}^B_{0,f}$ and $\mathcal{C}^B_{0,f}$ are the two segments on the new branch cut with opposite orientations. The contour $-\mathcal{C}^B_{0,f}$ points towards the branch point and $\mathcal{C}^B_{0,f}$ points away from the branch point.
3. Using that $e^{ikx-\omega(k)t} \int_t^\infty e^{\omega(k)s} g_0(s)\, \mathrm{d}s$ is bounded and analytic in $\tilde{D}$, we can replace $\tilde{g}_0(\omega(k), t)$ with $\tilde{g}_0(\omega(k), \infty)$,

$$
\begin{aligned}
B_0|_{D_2^+} =& \frac{1}{2\pi} \int_{\partial D_2^+} e^{ikx-\omega(k)t} (\tilde{\nu}_2^2(k) - k^2) \tilde{g}_0(\omega(k), t)\, \mathrm{d}k \\
=& \frac{1}{2\pi} \int_{\mathcal{C}^B_{0,a} \cup \mathcal{C}^B_{0,b} \cup \mathcal{C}^B_{0,e} \cup \mathcal{C}^B_{0,c}} e^{ikx-\omega(k)t} (\tilde{\nu}_2^2(k) - k^2) \tilde{g}_0(\omega(k), \infty)\, \mathrm{d}k \\
& - \frac{1}{2\pi} \int_{\mathcal{C}^B_{0,f}} e^{ikx-\omega(k)t} \tilde{\nu}_2^2(k^-) \tilde{g}_0(\omega(k), \infty)\, \mathrm{d}k + \frac{1}{2\pi} \int_{\mathcal{C}^B_{0,f}} e^{ikx-\omega(k)t} \tilde{\nu}_2^2(k^+) \tilde{g}_0(\omega(k), \infty)\, \mathrm{d}k,
\end{aligned}
$$

where k^+ and k^- denote the limit from the left/right of the curve, respectively.

4. The integral along $\mathcal{C}_{0,a}^{B}$ is decomposed into two parts to maximize decay along the steepest-descent direction:

$$\begin{aligned}&\int_{\mathcal{C}_{0,a}^{B}} e^{ikx-\omega(k)t}(\tilde{\nu}_2^2(k)-k^2)\tilde{g}_0(\omega(k),\infty)\,\mathrm{d}k\\&\quad=\int_{\mathcal{C}_{0,a}^{B}} e^{ikx-\omega(k)t}(\tilde{\nu}_2^2(k)-k^2)\tilde{g}_0^{c}(\omega(k),t)\,\mathrm{d}k\quad+\int_{\mathcal{C}_{0,d}^{B}} e^{ikx-\omega(k)t}(\tilde{\nu}_2^2(k)-k^2)\tilde{g}_0(\omega(k),t)\,\mathrm{d}k.\end{aligned}$$

5. We obtain

$$\begin{aligned}B_0|_{D_2^+}=&\frac{1}{2\pi}\int_{\mathcal{C}_{0,a}^{B}} e^{ikx-\omega(k)t}(\tilde{\nu}_2^2(k)-k^2)\tilde{g}_0^{c}(\omega(k),t)\,\mathrm{d}k+\frac{1}{2\pi}\int_{\mathcal{C}_{0,d}^{B}} e^{ikx-\omega(k)t}(\tilde{\nu}_2^2(k)-k^2)\tilde{g}_0(\omega(k),t)\,\mathrm{d}k\\&+\frac{1}{2\pi}\int_{\mathcal{C}_{0,b}^{B}} e^{ikx-\omega(k)t}(\tilde{\nu}_2^2(k)-k^2)\tilde{g}_0(\omega(k),\infty)\,\mathrm{d}k\\&+\frac{1}{2\pi}\int_{\mathcal{C}_{0,e}^{B}\cup\mathcal{C}_{0,c}^{B}} e^{ikx-\omega(k)t}(\tilde{\nu}_2^2(k)-k^2)\tilde{g}_0(\omega(k),\infty)\,\mathrm{d}k\\&+\frac{1}{2\pi}\int_{-\mathcal{C}_{0,f}^{B}} e^{ikx-\omega(k)t}\tilde{\nu}_2^2(k^+)\tilde{g}_0(\omega(k),\infty)\,\mathrm{d}k+\frac{1}{2\pi}\int_{\mathcal{C}_{0,f}^{B}} e^{ikx-\omega(k)t}\tilde{\nu}_2^2(k^+)\tilde{g}_0(\omega(k),\infty)\,\mathrm{d}k.\end{aligned}$$

The integrals along $\mathcal{C}_{0,b}^{B}, \mathcal{C}_{0,d}^{B}, -\mathcal{C}_{0,f}^{B}$ and $\mathcal{C}_{0,f}^{B}$ are computed using Clenshaw–Curtis quadrature, and the integrals along $\mathcal{C}_{0,a}^{B}, \mathcal{C}_{0,c}^{B}$ and $\mathcal{C}_{0,e}^{B}$ are computed using Levin's method. The contour integral $B_0|_{D_1^+}$ is deformed symmetrically.

5.1.3 *Improving the accuracy near the branch point.* Since $\tilde{\nu}_2(k)$ is not differentiable at the branch point $k_2 = 2/\sqrt{3}$, Clenshaw–Curtis quadrature loses spectral accuracy for the integrals along $-\mathcal{C}_{0,f}^{B}$, $\mathcal{C}_{0,f}^{B}$ and $\mathcal{C}_{0,b}^{B}$ in the critical case $x = 3t$. With the change of variables $s^2 = k - k_2$, we get

$$\hat{\nu}_2(s) := \nu_2(s^2 + k_2) = (-2\sqrt{3} - 3s^2 - i3^{5/4}s\sqrt{4 + \sqrt{3}s^2})/6.$$

The new symmetry $\hat{\nu}_2(s)$ is smooth near $s = 0$. Clenshaw–Curtis quadrature maintains spectral accuracy for the integrals on $\mathcal{C}_{0,b}^{B}$ and $\mathcal{C}_{0,f}^{B}$ after this change of variables.

5.1.4 *Improving the accuracy near the saddle point.* Large numerical rounding errors can arise if the parametrization along $\mathcal{C}_{0,b}^{B}$ is not smooth. For instance, the parametrization of $\mathcal{C}_{0,b}^{B}$ using Re (k) by mapping the curve to the real line has a square root singularity at the saddle point. Other than seeking an optimal parametrization we use line segments to approximate the curve near the saddle point.

5.2 *Numerical examples*

Consider the Dirichlet boundary condition $g_0(t) = te^{-t}$, the homogeneous initial condition $q_0(x) = 0$ and the Neumann boundary condition $g_1(t) = 0$. The solution to (21) is shown in Fig. 19. For small time

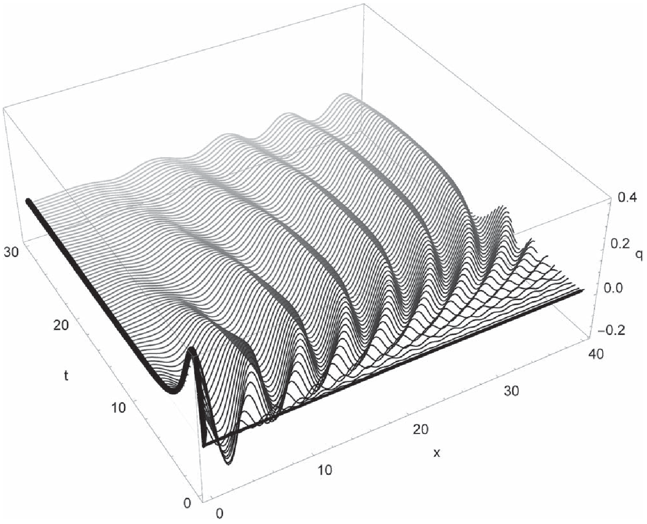

FIG. 19. The numerical solution of equation (21) with $q_0(x) = 0$, $g_0(t) = te^{-t}$, $g_1(t) = 0$. The bold curves are the initial and Dirichlet boundary conditions. For small t dispersive waves emanate from the boundary while the waves start to turn back following the advection as t grows.

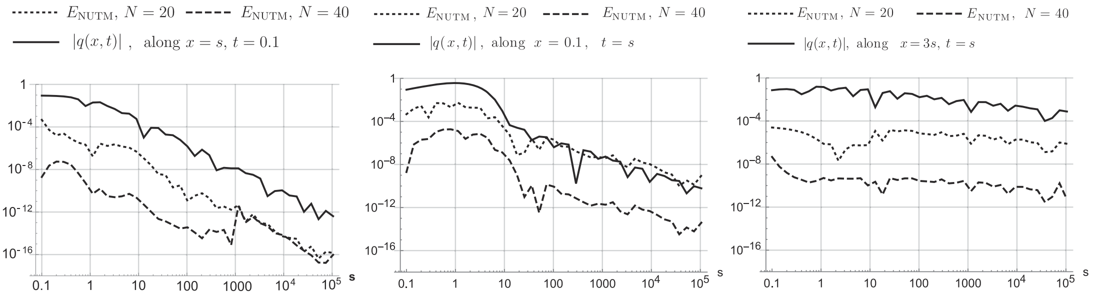

(a) (b) (c)

FIG. 20. The absolute error E_{NUTM} of the numerical solution to (21) along (a) $x = s, t = 0.1$, (b) $x = 0.1, t = s$, (c) $x = 3s, t = s$ for $s \in [0.1, 10^5]$. The computation using $N = 20$ points for each segment in the contour (dotted) and using $N = 40$ points for each segment in the contour (dashed) are plotted.

the dispersive waves emanate from the boundary and the solution looks similar to Fig. 13. As t grows the advection dominates and the waves turn back to the boundary. The absolute error and the magnitude of the solution evaluated along (a) $t = 0.1$, (b) $x = 0.1$, (c) $x = 3t$ are shown in Fig. 20. The errors shown in dotted curves are computed with $N = 20$ collocation points for each part of the contour in B_0, while the errors shown in solid curves are computed with $N = 40$ collocation points. The absolute errors tend to zero as x, t increase. To demonstrate spectral accuracy, the absolute errors E_{NUTM} evaluated at $x = 1, 3, 5$, $t = 1$ are plotted against the number of collocation points per segment in Fig. 21. With the change of variables used in Section 5.1.3 the NUTM remains spectrally accurate, even when the branch point is on the contour of integration.

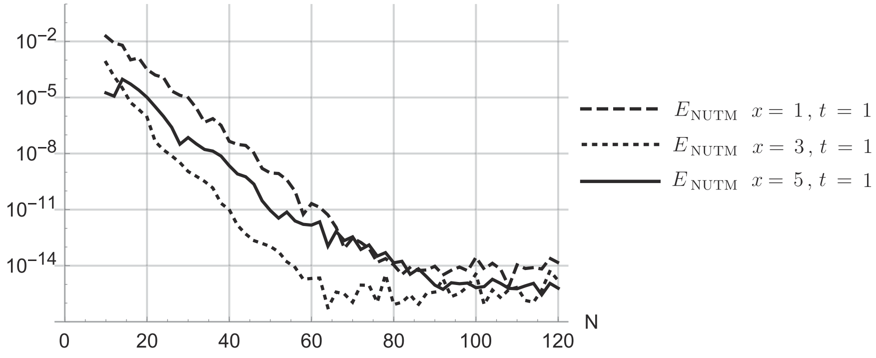

FIG. 21. The absolute error E_{NUTM} against the number of collocation points N per segment: computed with $x = 1, t = 1$ (dashed), $x = 3, t = 1$ (dotted) and $x = 5, t = 1$ (solid). The truncation tolerance is 10^{-15} for this example.

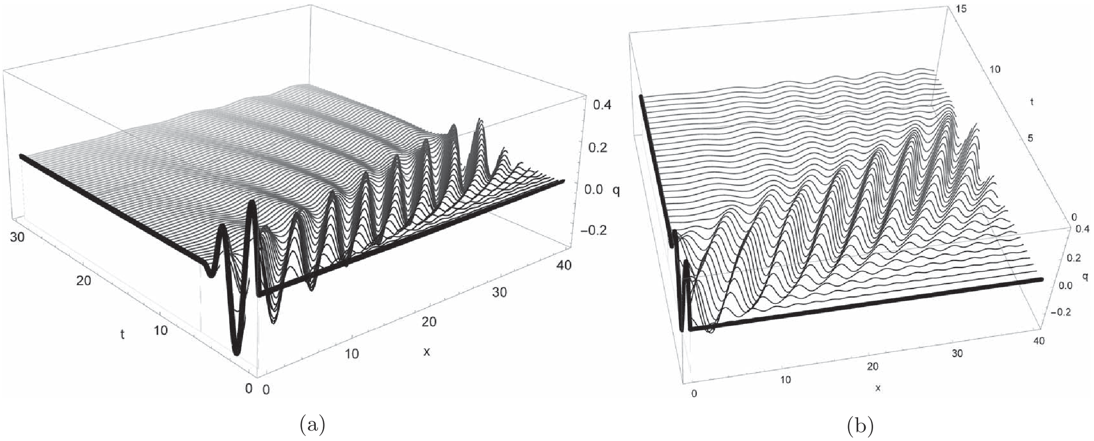

(a)

(b)

FIG. 22. The numerical solution of (21) with $g_0 = \sin(2t)\phi(t/(2\pi))$ with $\phi(t)$ defined in (23). The bold curves are the initial and Dirichlet boundary conditions. For small t, dispersive waves emanate from the boundary, but the waves start to turn back because of advection as t grows. Panel (a) shows the solution for $x \in [0, 40]$, $t \in [0, 30]$. Panel (b) shows the solution from a different angle in a shorter time interval $t \in [0, 15]$.

All our examples use boundary conditions with transforms that can be computed explicitly. This is to allow us to estimate the error of our method by comparing with the built-in integration routine in Mathematica. To show the NUTM is not limited to this, in Fig. 22, we show a plot of the solution $q(x, t)$ with $g_0(t) = \sin(2t)\phi(t/(2\pi))$, where

$$\phi(t) = \begin{cases} \exp(-1/(1-t^2)) & |t| \le 1, \\ 0 & |t| > 1. \end{cases} \tag{23}$$

The initial data and the Neumann data are zero. We see a similar wave pattern as in Fig. 19 with dispersive waves propagating in the positive x direction, before turning back.

6. Summary of the steps in the NUTM

1. For PDEs of type

$$q_t + \omega(-i\partial_x)q = 0$$

we construct the solution formula using the UTM.

2. The solution formula from the UTM requires transforms of the known initial and boundary data

$$\begin{aligned}
\hat{q}_0(k) &= \int_0^\infty e^{-ikx} q_0(x,0)\,\mathrm{d}x,\\
\tilde{g}_0(\omega(k),\infty) &= \int_0^\infty e^{\omega(k)s} q(0,s)\,\mathrm{d}s,\\
&\vdots\\
\tilde{g}_{p-1}(\omega(k),\infty) &= \int_0^\infty e^{\omega(k)s} \frac{\partial^{p-1} q}{\partial x^{p-1}}(0,s)\,\mathrm{d}s.
\end{aligned}$$

For most k values used on the deformed contour these integrals are oscillatory. We apply Levin's method to compute these integrals.

3. The solution formula depends on (x,t) explicitly through $e^{ikx-\omega(k)t}$. Generally, each connected component of D^+ contains saddle points. The contour ∂D^+ is deformed to pass through the saddle points along the steepest descent directions until it hits the boundary of $\tilde{D}$ (a slightly enlarged version of D^+), where the transforms of the initial and boundary data are analytic. The size of $\tilde{D}$ is determined by the decay rate of the initial and boundary data. The path follows $\partial\tilde{D}$ in the same direction as ∂D^+. The contour deformations may be impacted by singularities such as branch cuts and poles.

4. The integrals along the steepest descent direction are nonoscillatory and they are computed using standard quadrature rules. The integrals along $\partial\tilde{D}$ are oscillatory and they are computed using Levin's method.

Acknowledgements

Any opinions, findings, and conclusions or recommendations expressed in this material are those of the authors, and do not necessarily reflect the views of the funding sources.

Funding

US National Science Foundation (NSF-DMS-1522677 to B.D. and X.Y., NSF-DMS-1753185 to T.T., NSF-DMS-1945652 to T.T.).

References

de Barros, Colbrook, M. J. & Fokas, A. S. (2019) A hybrid analytical-numerical method for solving advection-dispersion problems on a half-line. *Int. J. Heat Mass Transfer*, **139**, 482–491.

Deconinck, B., Trogdon, T. & Vasan, V. (2014) The method of Fokas for solving linear partial differential equations. *SIAM Rev.*, **56**, 159–186.

Deconinck, B., Trogdon, T. & Yang, X. (2019) Numerical inverse scattering for the sine-Gordon equation. *Phys. D*, **399**, 159–172.

Flyer, N. & Fokas, A. S. (2008) A hybrid analytical-numerical method for solving evolution partial diffrerential equations. I. The half-line. *Proc. R. Soc. A*, **464**, 1823–1849.

Fokas, A. S. (1997) A unified transform method for solving linear and certain nonlinear PDEs. *Proc. R. Soc. A*, **453**, 1411–1443.

Fokas, A. S. (2002a) A new transform method for evolution partial differential equations. *IMA J. Appl. Math.*, **67**, 559–590.

Fokas, A. S. (2002b) Integrable nonlinear evolution equations on the half-line. *Comm. Math. Phys.*, **230**, 1–39.

Fokas, A. S. (2005) The nonlinear Schrödinger equation on the half-line. *Nonlinearity*, **18**, 1771–1882.

Fokas, A. S. (2008) *A Unified Approach to Boundary Value Problems*. Philadelphia, PA: SIAM.

Fokas, A. S., Flyer, N., Smitheman, S. A. & Spence, E. A. (2009) A semi-analytical numerical method for solving evolution and elliptic partial differential equations. *J. Comput. Appl. Math.*, **227**, 59–74.

Gibbs, A., Hewett, D., Huybrechs, D. & Parolin, E. (2020) Fast hybrid numerical-asymptotic boundary element methods for high frequency screen and aperture problems based on least-squares collocation. *SN Partial Differ. Equat. Appl.*, **1**, Article number 21.

Huybrechs, D. & Gibbs, A. PathFinder: a toolbox for oscillatory integrals by deforming into the complex plane. Available at https://github.com/AndrewGibbs/PathFinder.

Iserles, A., Norsett, S. P. & Olver, S. (2006) Highly oscillatory quadrature: the story so far. *Numerical Mathematics and Advanced Applications* (A. de Castro, D. Gómez, P. Quintela, & P. Salgado eds). Berlin, Heidelberg: Springer, pp. 97–118.

Kesici, E., Pelloni, B., Pryer, T. & Smith, D. (2018) A numerical implementation of the unified Fokas transform for evolution problems on a finite interval. *European J. Appl. Math.*, **29**, 543–567.

Miller, P. D. (2006) *Applied Asymptotic Analysis*. Providence, RI: AMS.

Olver, S. & Townsend, A. (2012) A fast and well-conditioned spectral method. *SIAM Rev.*, **55**, 462–489.

Papatheodorou, T. S. & Kandili, A. N. (2009) Novel numerical techniques based on Fokas transforms, for the solution of initial boundary value problems. *J. Comput. Appl. Math.*, **227**, 75–82.

Trefethen, L. N. (2008) Is Gauss quadrature better than Clenshaw–Curtis? *SIAM Rev.*, **50**, 67–87.

Trogdon, T. (2015) A unified numerical approach for the nonlinear Schrödinger equations. *Unified Transform Method for Boundary Value Problems: Applications and Advances* (A. S. Fokas & B. Pelloni eds). Philadelphia, PA: SIAM, pp. 259–292.

Trogdon, T. & Biondini, G. (2019) Evolution partial differential equations with discontinuous data. *Quart. Appl. Math.*, **77**, 689–726.

Trogdon, T. & Olver, S. (2013) Numerical inverse scattering for the focusing and defocusing nonlinear Schrödinger equations. *Proc. R. Soc. Lond. A*, **469** 1–22.

Trogdon, T., Olver, S. & Deconinck, B. (2012) Numerical inverse scattering for the Korteweg-de Vries and modified Korteweg–de Vries equations. *Phys. D*, **241**, 1003–1025.

Uspensky, J. V. (1928) On the convergence of quadrature formulas related to an infinite interval. *Trans. Amer. Math. Soc.*, **30**, 542–559.

A. Appendix: The proof of uniform convergence of the NUTM applied to the heat equation

In this appendix, we prove the uniform convergence for Clenshaw–Curtis quadrature applied to the contour integrals for the heat equation in Section 3.2. We use the following result to estimate the error of Clenshaw–Curtis quadrature. The constant K for the integrals I_1, I_2 and B_0 is given in Theorem 2 and Theorem 3.

THEOREM 1. See Trogdon, 2015, for example.

Let $u(k;x,t)$ be so that for $m = 0, 1, \ldots, M$, $\partial_k^m u(k;x,t)$ are absolutely continuous for fixed x, t and satisfy $\sup_{k\in[-1,1]} \left|\partial_k^{M+1} u(k;x,t)\right| \leq K$ for all x, t. Define $i(u(\cdot;x,t)) = \int u(k;x,t)\,\mathrm{d}k$ and $i_n(u(\cdot;x,t))$ to be the approximation of $i(u(\cdot;x,t))$ obtained with Clenshaw–Curtis quadrature. Then $i_n(u(\cdot;x,t))$ converges to $i(u(\cdot;x,t))$ uniformly in x, t. More precisely, there exists $N > 0$ such that for $n > N$,

$$\sup_{x,t} \left|i(u(\cdot;x,t)) - i_n(u(\cdot;x,t))\right| \leq \frac{32K}{15M(2n+1-M)^M}.$$

In Theorem 2 and Theorem 3, we estimate the upper bound K for each part of the integral in (9). The uniform convergence is considered in the domain bounded away from $t = 0$ and $x = 0$. For $c > 0$ we define the region,

$$\Omega_c = \{(x,t) : \ x \geq c, \ t \geq c\}.$$

THEOREM 2. Uniform convergence of I_1 and I_2 in (9) for the heat equation.

For any $\delta, \epsilon, c > 0$, assume $q_0 \in C_\delta^\infty$ and let I_1^ϵ be the truncation of the integral[4]

$$I_1 = \frac{1}{2\pi} \int_{\mathcal{C}_1^I} e^{ikx-\omega(k)t} \hat{q}_0(k)\,\mathrm{d}k, \tag{A.1}$$

such that

$$\sup_{(x,t)\in\Omega_c} \left|I_1 - I_1^\epsilon\right| < C_1(q_0,\delta,c)\epsilon, \quad C_1(q_0,\delta,c) > 0.$$

Then Clenshaw–Curtis quadrature applied to I_1^ϵ converges uniformly on Ω_c. Hence, $\mathcal{C}_1^I = \{a + ih : a \in \mathbb{R}\}$ and $h = \min(x/2t, \delta)$ is as defined in Section 3.2.1. Similarly, with the same assumptions, let I_2^ϵ be the truncation of the integral

$$I_2 = -\frac{1}{2\pi} \int_{\mathcal{C}_2^I} e^{ikx-k^2 t} \hat{q}_0(-k)\,\mathrm{d}k, \tag{A.2}$$

such that

$$\sup_{(x,t)\in\Omega_c} \left|I_2 - I_2^\epsilon\right| < C_2(q_0,\delta,c)\epsilon, \quad C_2(q_0,\delta,c) > 0.$$

Then Clenshaw–Curtis quadrature applied to I_2^ϵ converges uniformly on Ω_c. Hence, $\mathcal{C}_2^I = \{a + ix/2t : a \in \mathbb{R}\}$.

THEOREM 3. Uniform convergence of B_0 in (9) for the heat equation.

---

[4] The truncation depends on the prescribed tolerance ϵ. As $\hat{q}_0$ is bounded on the contour, we can use the exponential to get a good choice for the truncation. See the proof for how the truncation is done.

For any $\gamma, \epsilon, c > 0$, assume $g_0 \in C^{\infty}_{\gamma}$ and let B_0^{ϵ} be the truncation of the integral[5]

$$B_0 = \frac{1}{\pi}\int_{\mathcal{C}^B_{0,a}} e^{ikx-k^2t} 2ik\tilde{g}_0(k^2,t)\,\mathrm{d}k + \frac{1}{2\pi}\int_{\mathcal{C}^B_{0,b}+\mathcal{C}^B_{0.c}} e^{ikx-k^2t} 2ik\tilde{g}_0(k^2,t)\,\mathrm{d}k, \tag{A.3}$$

such that

$$\sup_{(x,t)\in\Omega_c} \left|B_0 - B_0^{\epsilon}\right| < C(g_0,\gamma,c)\epsilon, \quad C(g_0,\gamma,c) > 0.$$

Then Clenshaw–Curtis quadrature applied to B_0^{ϵ} converges uniformly on Ω_c. The contour is defined in Section 3.2.3, where $\mathcal{C}^B_{0,a} = \{La + ix/2t : a \in [0,1], e^{-L^2t} = \epsilon\}$ is the horizontal segment of the contour, and $\mathcal{C}^B_{0,b} = \{L + ix/2t + L_2e^{i\pi/4}a : a \in [0,\infty), e^{-L_2x} = \epsilon\}$, $\mathcal{C}^B_{0,c} = \{-L + ix/2t + L_2e^{-i\pi/4}a : a \in (-\infty, 0], e^{-L_2x} = \epsilon\}$ are the oblique segments of the contour with given tolerance $\epsilon > 0$.

Proof of Theorem 2. For given tolerance $\epsilon > 0$, I_1 is truncated to I_1^{ϵ} of length $2L$ with $e^{-L^2t} = \epsilon$. We introduce the change of variables $k = La + ih$. The integral with $a > 1$ is cut off:

$$\begin{aligned}
I_1 =& \frac{Le^{-hx}}{2\pi}\int_{-\infty}^{\infty} e^{iLax-(La+ih)^2t}\hat{q}_0(La+ih)\,\mathrm{d}a \\
=& \frac{Le^{-hx}}{2\pi}\int_{-1}^{1} e^{iLax-(La+ih)^2t}\hat{q}_0(La+ih)\,\mathrm{d}a + \frac{Le^{-hx}}{2\pi}\int_{|a|>1} e^{iLax-(La+ih)^2t}\hat{q}_0(La+ih)\,\mathrm{d}a \\
=& I_1^{\epsilon} + \frac{Le^{-hx}}{2\pi}\int_{|a|>1} e^{iLax-(La+ih)^2t}\hat{q}_0(La+ih)\,\mathrm{d}a.
\end{aligned}$$

The second integral is dropped and the induced truncation error is bounded by

$$\begin{aligned}
\left|\frac{Le^{-hx}}{2\pi}\int_{|a|>1} e^{iLax-(La+ih)^2t}\hat{q}_0(La+ih)\,\mathrm{d}a\right| \leq& \frac{Le^{-hx}}{2\pi}\int_{|a|>1} \left|e^{iLax-(La+ih)^2t}\hat{q}_0(La+ih)\right|\,\mathrm{d}a \\
\leq& \frac{Le^{-hx}}{2\pi}\int_{|a|>1} e^{-L^2ta^2+h^2t}\left|\hat{q}_0(La+ih)\right|\,\mathrm{d}a \\
\leq& \|\hat{q}_0(\cdot+ih)\|_{\infty}\frac{Le^{-h(x-ht)}}{2\pi}\epsilon\int_{|a|>1} ae^{-L^2t(a^2-1)}\,\mathrm{d}a \\
\leq& \|\hat{q}_0(\cdot+ih)\|_{\infty}\frac{Le^{-h(x-ht)}}{2\pi}\epsilon\int_0^{\infty} e^{-L^2ts}\,\mathrm{d}s \\
\leq& \|\hat{q}_0(\cdot+ih)\|_{\infty}\frac{Le^{-h^2t}}{2\pi}\frac{\epsilon}{(-\ln\epsilon)}.
\end{aligned}$$

Since t is bounded from below L is bounded from above. The truncation error is therefore $\mathcal{O}(\epsilon)$, uniformly in $(x,t) \in \Omega_c$.

---

[5] As with Theorem 2, the truncation procedure is described in the proof.

Uniform convergence to I_1^ϵ requires the derivative of the integrand in I_1^ϵ to satisfy

$$\sup_{a\in[-1,1]} \frac{Le^{-hx}}{2\pi}\left|\partial_a^2\left(e^{iLax-(La+ih)^2t}\hat{q}_0(La+ih)\right)\right| \le M,$$

for all x, t. Notice that the derivatives of the exponential only introduce polynomial terms, and $\hat{q}_0(k)$ is bounded and analytic in $\{k : \operatorname{Im}(k) \le \delta\}$, which implies that $\partial_k\hat{q}_0(k)$ and $\partial_k^2\hat{q}_0(k)$ are bounded on the contour. It suffices to show

$$\begin{aligned}\sup_{a\in[-1,1]}\left|\partial_a^2\left(\frac{Le^{-hx}}{2\pi}\cdot e^{iLax-(La+ih)^2t}\hat{q}_0(La+ih)\right)\right| &\le \sup_{a\in[-1,1]}\left|\frac{Le^{-hx}}{2\pi}\cdot e^{iLax-(La+ih)^2t}P(a,Lx,L^2t,Lht)\right|\\ &= \sup_{a\in[-1,1]}\frac{Le^{-hx}}{2\pi}\cdot e^{-L^2ta^2+h^2t}\left|P(a,Lx,L^2t,Lht)\right|,\end{aligned}$$

where P is a polynomial with positive coefficients.

When $h = x/2t \le \delta$,

$$\begin{aligned}\sup_{a\in[-1,1]}\frac{Le^{-hx}}{2\pi}\cdot e^{-L^2ta^2+h^2t}\left|P(a,Lx,L^2t,Lht)\right| &= \sup_{a\in[-1,1]}\frac{Le^{-x^2/4t-L^2ta^2}}{2\pi}\left|P(a,Lx,L^2t,Lx/2)\right|\\ &\le \frac{e^{-x^2/4t}}{2\pi}Q(x^2/4t) \le M_1 < \infty,\end{aligned}$$

where Q is a polynomial with positive coefficients and we have used that L^2t is constant.

When $h = \delta < x/2t$,

$$\begin{aligned}\sup_{a\in[-1,1]}\frac{Le^{-hx}}{2\pi}\cdot e^{-L^2ta^2+h^2t}\left|P(a,Lx,L^2t,Lht)\right| &\le \sup_{a\in[-1,1]} e^{-\delta x/2-L^2ta^2}\left|P(a,Lx,L^2t,Lx/2)\right|\\ &\le \sup_{a\in[-1,1]} e^{-\delta x/2}Q_2(x) \le M_2 < \infty,\end{aligned}$$

where Q_2 is a polynomial with positive coeffcients. As a result the second derivative of the integrand of (A.1) is uniformly bounded by $M = \max(M_1, M_2)$ independent of x, t. Together with the smoothness of the integrand uniform convergence is obtained using Theorem 1. We skip the calculation for I_2 as it follows the calculation for I_1. □

Proof of Theorem 3. First, we prove the uniform convergence for the integral along $\mathcal{C}_{0,a}^B$. Introduce the change of variables $k = La + ix/2t$.

$$\begin{aligned}B_0|_{\mathcal{C}_{0,a}^B} &= \frac{1}{2\pi}\int_{\mathcal{C}_{0,a}^B} e^{ikx-k^2t}2k\tilde{g}_0(k^2,t)\,\mathrm{d}k\\ &= \frac{Le^{-x^2/2t}}{2\pi}\int_{-1}^{1} e^{iLax-(La+ix/2t)^2t}2(La+ix/2t)\tilde{g}_0((La+ix/2t)^2,t)\,\mathrm{d}a\\ &= \frac{Le^{-x^2/4t}}{\pi}\int_{-1}^{1} e^{-L^2ta^2}(La+ix/2t)\int_0^t e^{(La+ix/2t)^2s}g(s)\,\mathrm{d}s\,\mathrm{d}a.\end{aligned}$$

Using Theorem 1, uniform convergence requires the boundedness of the second derivative of the integrand

$$B_a = \sup_{a\in[0,1]} \frac{Le^{-x^2/4t}}{\pi} \left| \partial_a^2 e^{-L^2ta^2}(La+ix/2t)\int_0^t e^{(La+ix/2t)^2 s-\gamma s} g(s)e^{\gamma s}\,\mathrm{d}s \right| \le M,$$

for all $(x,t)\in\Omega_c$. Since $\|ge^{\gamma(\cdot)}\|_\infty < \infty$, after a lengthy computation,

$$B_a \le \sup_{a\in[0,1]} \frac{\|ge^{\gamma(\cdot)}\|_\infty}{|-4a^2t^2+4\gamma t^2-4iatx+x^2|^3}\left(e^{-a^2t-x^2/4t}P_1 + e^{-\gamma t-x^2/2t}P_2\right),$$

where P_1, P_2 are polynomials in x, t and a, with positive coefficients, and the growth for large x, t is controlled by the exponential and the denominator in front of P_1, P_2. As a result $B_a \le M$ and the integral on $\mathcal{C}^B_{0,a}$ is computed with uniform accuracy.

Lastly, we show the uniform convergence for the integral along the oblique segment $\mathcal{C}^B_{0,b}$. The proof for the integral along $\mathcal{C}^B_{0,c}$ follows directly by symmetry. We introduce the change of variables $k = L + ix/2t + L_2(1+i)a$. The integral with $a > 1$ is separated:

$$\begin{aligned} B_0|_{\mathcal{C}^B_{0,b}} &= \frac{L_2(1+i)}{\pi}\left(\int_0^1 + \int_1^\infty\right) e^{ikx-k^2t} k\tilde{g}_0(k^2,t)\Big|_{k=L+ix/2t+L_2(1+i)a}\,\mathrm{d}a \\ &= B_0^\epsilon|_{\mathcal{C}^B_{0,b}} + \frac{L_2(1+i)}{\pi}\int_1^\infty e^{ikx-k^2t}k\tilde{g}_0(k^2,t)\Big|_{k=L+ix/2t+L_2(1+i)a}\,\mathrm{d}a. \end{aligned}$$

The second integral is dropped and the induced truncation error is bounded by

$$\begin{aligned} \left| B_0|_{\mathcal{C}^B_{0,b}} - B_0^\epsilon|_{\mathcal{C}^B_{0,b}} \right| &\le \frac{L_2 e^{-L^2t-x^2/(4t)}}{\pi}\int_1^\infty \left| e^{-2LL_2ta}\left(Lt + L_2ta + \frac{x}{2t}\right)\tilde{g}_0((L+ix/2t+L_2(1+i)a)^2,t)\right|\,\mathrm{d}a \\ &\le \frac{L_2 e^{-x^2/(4t)}\|g_0e^{\gamma(\cdot)}\|_\infty}{\pi}\int_1^\infty \left| \left(Lt+L_2ta+\frac{x}{2t}\right)\frac{\left(e^{-L_2xa-x^2/(4t)-\gamma t} - e^{-L^2t-2LL_2ta}\right)}{(L-x/(2t))(2aL_2+L+x/(2t))-\gamma}\right|\,\mathrm{d}a \\ &\le e^{-x^2/(4t)}\|g_0e^{\gamma(\cdot)}\|_\infty\left(e^{-L_2x-\gamma t}P_3 + e^{-L^2t-2LL_2t}P_4\right), \end{aligned}$$

where P_3, P_4 are polynomials of x, t with positive coefficients. Since the decaying exponentials dominate the growth of the polynomial the truncation error is $\mathcal{O}(\epsilon)$, uniformly in $(x,t)\in\Omega_c$ with $e^{-L_2x} = \epsilon$ and $e^{-L^2t} = \epsilon$. Using Theorem 1 uniform convergence requires the boundedness of the second derivative of the integrand

$$B_b = \sup_{a\in[0,1]} \frac{L_2e^{i\pi/4}}{2\pi}\left|\partial_a^2\left(e^{ikx-k^2t}2k\tilde{g}_0(k^2,t)\Big|_{k=L+ix/2t+L_2e^{i\pi/4}a}\right)\right| \le M_b,$$

for all x, t. After computing the derivatives

$$B_b \le \sup_{a\in[0,1]} \frac{\|g_0e^{\gamma(\cdot)}\|_\infty}{|4\gamma t^2-(2Lt+(2+2i)aL_2t+ix)^2|^3}\left(e^{-L^2t-2aLL_2t-x^2/(4t)}P_5 + e^{-\gamma t-aL_2x-x^2/(2t)}P_6\right),$$

where P_5, P_6 are polynomials of x, t, a with positive coefficients. The poles are removable since the integrand is analytic in k. In this case the exponentials dominate the growth of the polynomial. Hence,

$B_b \leq M$. The second derivative of the integrand of (A.1) is uniformly bounded by M, independent of x, t. Together with the smoothness of the integrand uniform convergence is obtained using Theorem 1. □